Low-ionization iron-rich broad absorption-line quasar SDSS J 1652+2650: physical conditions in the ejected gas from excited Fe II and metastable He I

S. A. Balashev [1]⋆ C. Ledoux,[2] P. Noterdaeme,[3,4] P. Boissé,[4] J.-K. Krogager [5] S. López [6]
and K. N. Telikova [1]

[1]*Department of Theoretical Astrophysics, Ioffe Institute, Polyteknicheskaya 26, Saint Petersburg 194021, Russia*
[2]*European Southern Observatory, Alonso de Córdova 3107, Vitacura, Casilla 19001, Santiago, Chile*
[3]*Franco-Chilean Laboratory for Astronomy, IRL 3386, CNRS and U. de Chile, Casilla 36-D, Santiago, Chile*
[4]*Institut d'Astrophysique de Paris, CNRS-SU, UMR 7095, 98bis bd Arago, F-75014 Paris, France*
[5]*Centre de Recherche Astrophysique de Lyon, UMR 5574, 9 avenue Charles André, F-69230 Saint-Genis-Laval, France*
[6]*Departamento de Astronomía, Universidad de Chile, Casilla 36-D, Santiago, Chile*

ABSTRACT

We present high-resolution VLT/UVES spectroscopy and a detailed analysis of the unique broad absorption-line system towards the quasar SDSS J 165252.67+265001.96. This system exhibits low-ionization metal absorption lines from the ground states and excited energy levels of Fe II and Mn II, and the meta-stable $2\,^3S$ excited state of He I. The extended kinematics of the absorber encompasses three main clumps with velocity offsets of -5680, -4550, and -1770 km s^{-1} from the quasar emission redshift, $z = 0.3509 \pm 0.0003$, derived from [O II] emission. Each clump shows moderate partial covering of the background continuum source, $C_f \approx [0.53; 0.24; 0.81]$. We discuss the excitation mechanisms at play in the gas, which we use to constrain the distance of the clouds from the active galactic nucleus (AGN) as well as the density, temperature, and typical sizes of the clouds. The number density is found to be $n_{\rm H} \sim 10^4$ cm^{-3} and the temperature $T_{\rm e} \sim 10^4$ K, with longitudinal cloudlet sizes of $\gtrsim 0.01$ pc. CLOUDY photoionization modelling of He I⋆, which is also produced at the interface between the neutral and ionized phases, assuming the number densities derived from Fe II, constrains the ionization parameter to be $\log U \sim -3$. This corresponds to distances of a few 100 pc from the AGN. We discuss these results in the more general context of associated absorption-line systems and propose a connection between FeLoBALs and the recently identified molecular-rich intrinsic absorbers. Studies of significant samples of FeLoBALs, even though rare per se, will soon be possible due to large dedicated surveys paired with high-resolution spectroscopic follow-ups.

Key words: line: formation – galaxies: active – quasars: absorption lines – quasars: individual: SDSS J 165252.67+265001.96, NVSS J 235953−124148.

1 INTRODUCTION

A key characteristic of around 20 per cent of optically selected quasars is the occurrence of broad absorption-line (BAL) systems along the line of sight to the quasar (Tolea, Krolik & Tsvetanov 2002; Hewett & Foltz 2003; Reichard et al. 2003; Knigge et al. 2008; Gibson et al. 2009). BAL systems are typically associated with highly ionized metals, e.g. C IV and O VI, and their wide kinematic spreads, velocity offsets, and partial covering factors all indicate that they are produced by outflowing gas. Observations of such outflows provide a direct test of quasar feedback models.

One-tenth of BAL systems show associated wide Mg II absorption (Trump et al. 2006) and are called low-ionization BALs (hereafter LoBALs). An even smaller fraction, totalling only ~ 0.3 per cent of the global quasar population, in addition, exhibits Fe II absorption and is hence called FeLoBALs. A qualifying feature of FeLoBALs is the detection of Fe II in its various fine-structure energy levels of the

lowest electronic states. These levels may be excited by collisions or UV pumping, and their relative abundance can provide robust estimates of critical physical parameters. Interestingly, the modelling of FeLoBALs indicates they contain some neutral gas and likely occur at the interface between the ionized and neutral media (Korista et al. 2008). Another feature of FeLoBALs, which was gradually recognized, is the presence of absorption lines corresponding to transitions from the first excited level of neutral helium, He I⋆ (Arav et al. 2001; Aoki et al. 2011; Leighly, Dietrich & Barber 2011). This is observed in FeLoBALs but also more generally in LoBALs (Liu et al. 2015). These lines have also been detected in the host galaxies of a few gamma-ray bursts (Fynbo et al. 2014). He I⋆ is predominantly populated by recombination of He II and the measured column densities of He I⋆ provide a measure of the total column density of the ionized medium. This can constrain the physical conditions in the outflowing gas and determine the total mass budget to draw a more complete physical picture of quasar activity. For example, rapid cooling followed by the phase transition and subsequent condensation in an outflowing medium can result in the escape of small chunks of the medium from the outflowing
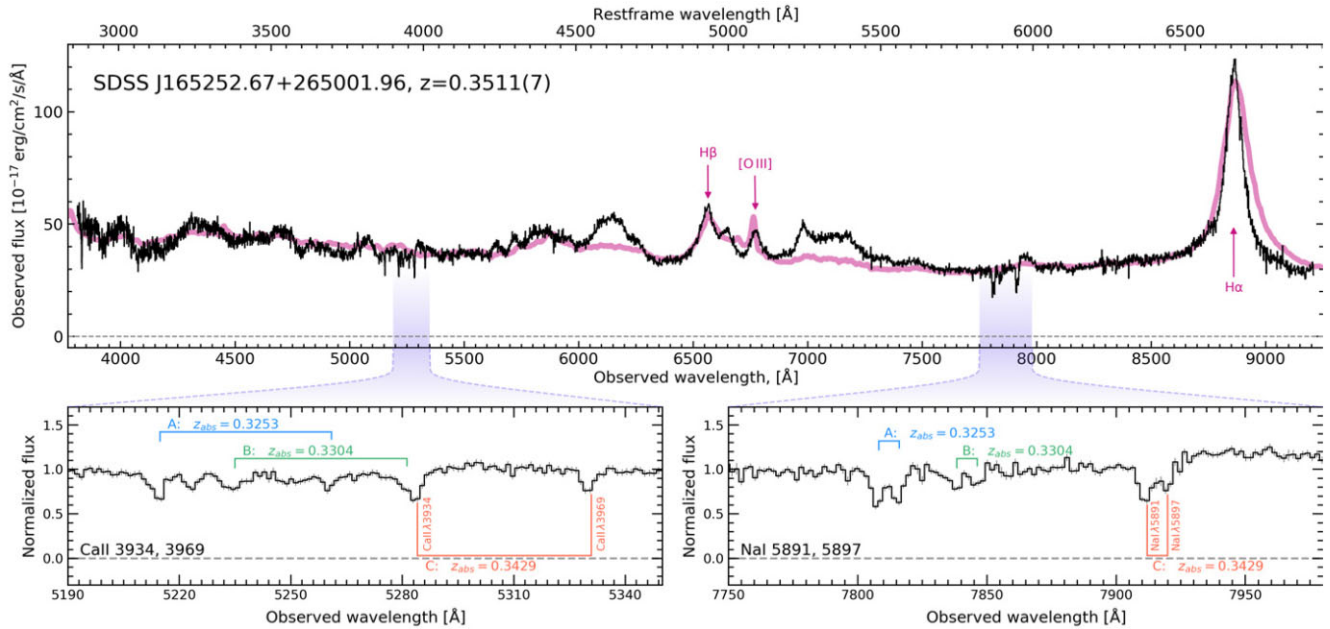
Figure 1. SDSS spectrum of J 1652+2650. The top panel shows the full range of SDSS spectrum plotted by the black line. The quasar emission lines are marked by pink arrows, while the pink line represents the composite QSO spectrum reddened by dust (see Section 3.1). The bottom panels show a zoom view of Ca II and Na I absorption line regions (these lines were used to pre-select J 1652+2650 from SDSS data base, see Section 2). The red, green, and blue lines indicate absorption line complexes that were resolved using UVES spectrum, see Section 3.2.

gas. Such cloudlets can precipitate back on to the central engine and sustain the formation of the broad-line region around the central powering source (Elvis 2017).

Because the incidence rate of FeLoBALs in quasars is low, only a small sample of such systems was found in the Sloan Digital Sky Survey (SDSS) data base (e.g. Trump et al. 2006; Farrah et al. 2012; Choi et al. 2022). Most importantly, only about a dozen such systems was studied so far by means of high-resolution near-UV and visual spectroscopy, i.e. Q 0059−2735 (Hazard et al. 1987; Wampler, Chugai & Petitjean 1995; Xu et al. 2021), Q 2359−1241 (Arav et al. 2001, 2008), FIRST 104459.6+365605 (Becker et al. 2000; de Kool et al. 2001), FBQS 0840+3633 (Becker et al. 1997; de Kool et al. 2002b), FIRST J 121442.3+280329 (Becker et al. 2000; de Kool et al. 2002a), SDSS J 030000.56+004828.0 (Hall et al. 2003), SDSS J 0318−0600 (Bautista et al. 2010; Dunn et al. 2010), AKARI J 1757+5907 (Aoki et al. 2011), PG 1411+442 (Hamann et al. 2019), SDSS J 2357−0048 (Byun, Arav & Hall 2022b), SDSS J 1439−0106 (Byun, Arav & Walker 2022a), SDSS J 0242+0049 (Byun, Arav & Hall 2022c), SDSS J 1130+0411 (Walker, Arav & Byun 2022), Mrk 231 (Boroson et al. 1991; Smith et al. 1995; Veilleux et al. 2016), and NGC 4151 (Crenshaw et al. 2000; Kraemer et al. 2001). Among these, only a few systems exhibit mild line saturation and overlapping, which allow one to resolve the fine-structure lines and therefore derive robust constraints on the gas physical conditions (Arav et al. 2008). Moreover, each previously studied system appears to be fairly specific, i.e. FeLoBALs show a broad range of properties, which means any new observation and detailed analysis potentially bring new valuable clues to understanding the physics and environmental properties of active galactic nucleus (AGN) outflows.

In this paper, we report the serendipitous discovery of a multiclump FeLoBAL towards SDSS J 165252.67+265001.96, which we refer to in the following text as J 1652+2650. We present high-quality VLT/UVES data of this quasar and the spectroscopic analysis of the absorption system and discuss the excitation mechanisms at play in

the gas. Our goal is to infer the physical properties of FeLoBAL clouds and estimate their distance from the central engine.

2 OBSERVATIONS AND DATA REDUCTION

We selected the bright quasar J 1652+2650 ($B = 18.2$; $V = 17.7$; $z_{em} = 0.35$; Véron-Cetty & Véron 2010) with the primary goal to search for CN, CH, and CH$^+$ molecules in absorption based on the detection of strong associated Na I lines at $z \approx 0.33$ in the SDSS spectrum (Negrete et al. 2018; Pâris et al. 2018), which is shown in Fig. 1. We observed the target in visitor mode on the night of 2019 July 27, with UVES, the Ultraviolet and Visual Echelle Spectrograph (Dekker et al. 2000) installed at the Nasmyth-B focus of the ESO Very Large Telescope Unit-2, Kueyen. The total on-source integration time was 4 h, subdivided evenly into three exposures taken in a row. The instrumental set-up used Dichroic beam splitter #1 and positioning of the cross-dispersers at central wavelengths of 390 and 590 nm in the blue and red spectroscopic arms, respectively. In each arm, the slit widths were fixed to 1 arcsec and CCD pixels were binned 2×2. While observing, the weather conditions were excellent with clear sky transparency and a measured Differential Image Motion Monitor (Sarazin & Roddier 1990) seeing of 0.6 arcsec. Despite a relatively high airmass (1.63–1.97), the source was recorded on the detectors with a spatial PSF trace of only 1.1 arcsec full width at half-maximum (FWHM) in the blue (1.0 arcsec FWHM in the red).

The raw data from the telescope were reduced offline applying the recipes of the UVES pipeline v5.10.4 running on the ESO Reflex platform. During this process, the spectral format of the data was compared to a physical model of the instrument, to which a slight CCD rotation was applied ($-0.05°$ in the blue; $+0.05°$ in the red). ThAr reference frames acquired in the morning following the observations were used to derive wavelength-calibration solutions, which showed residuals of 1.53 mÅ RMS in the blue (4.25 mÅ RMS in the red). The object and sky spectra were extracted simultaneously

and optimally, and cosmic-ray hits were removed efficiently using a κ-σ clipping factor of 5. The wavelength scale was converted to the helio-vacuum rest frame. Individual 1D exposures were then scaled and combined together by weighing each pixel by its S/N. The S/N of the final science product is ∼15 per pixel at 325 nm < λ_{obs} < 455 nm and ∼32 per pixel at 490 nm < λ_{obs} < 690 nm. With a delivered resolving power of 50 000, the instrumental line-spread function is 6 km s^{-1} FWHM.

3 DATA ANALYSIS

3.1 Quasar spectrum and systemic redshift

J 1652+2650 exhibits moderate reddening. Based on the SDSS spectrum, shown in Fig. 1, and using the Type I quasar template from Selsing et al. (2016), we followed a procedure similar to that employed by Balashev et al. (2017, 2019) and derived that $A_V \approx$ 1.2, assuming standard galactic extinction law (Fitzpatrick & Massa 2007). This is quite large compared to intervening quasar absorbers, e.g. DLAs (Murphy & Bernet 2016). We also note that this quasar shows iron-emission line complexes in the spectral regions around 4600 and 5300 Å in the quasar rest frame, which are enhanced by a factor of ∼4 relative to the fiducial quasar template (see Fig. 1).

To determine the quasar emission redshift accurately, we followed the recommendations of Shen et al. (2016) that Ca II and [O II] should be considered the most reliable systemic-redshift indicators. In the case of J 1652+2650, the blue side of the Ca II profile is affected by strong self-absorption, so we are left with [O II], which according to Shen et al. (2016) is not significantly shifted relative to Ca II. Based on a single-component Gaussian fit, we measured $z_{em} = 0.3511(7)$ when considering the [O II],$\lambda3727.092$ transition line alone, and $z_{em} = 0.3506(7)$ when using the mean wavelength of the [O II],$\lambda\lambda3727.092,3729.875$ doublet. This translates into $z_{em} = 0.3509 \pm 0.0003$, which we consider as our most-accurate determination of the quasar systemic redshift. The H β emission line is observed at a redshift of $z \approx 0.3494$, implying a velocity blue-shift of $\Delta V \sim -330$ km s^{-1} relative to [O II]. This is consistent with the findings of Shen et al. (2016) using their own sample.

3.2 Absorption-line system overview

The FeLoBAL[1] on the line of sight to J 1652+2650 consists of multiple prominent absorption lines from Mg II, Ca II, He I* (i.e. the meta-stable excited state 2^3S), Mg I, Fe II, and Mn II, all covered by the UVES spectrum. The system is composed of three main, kinematically detached absorption-line complexes,[2] i.e. at $z_{abs} =$ 0.32531 ($\Delta V \approx -5680$ km s^{-1}), 0.33043 ($\Delta V \approx -4550$ km s^{-1}), and 0.34292 ($\Delta V \approx -1770$ km s^{-1}), where the reddest and bluest clumps exhibit the strongest Mg II and Ca II absorption overall (see

Fig. 2). In the following text, we refer to these three complexes as *A*, *B*, and *C*, in order of increasing redshift. Each complex has at least a few velocity components resolved by eye within its own profile. Weak absorption is also visible in Mg II at $z_{abs} = 0.3357$ ($\Delta V \approx -3390$ km s^{-1}) and, tentatively, also in Ca II $\lambda3934$.

Fe II,$\lambda\lambda2586,2600$ ground-state absorption lines as well as lines from the fine-structure energy levels of the two LS states 3d^{6}4s a^{6}D (ground) and 3d^{6}4s a^{4}D (second excited state, which is encompassing the Fe II^{9*}–Fe II^{12*} levels) are detected in this system (see Figs A2, A3, and A4). Transition lines from the first excited LS state 3d^7 a^{4}F (i.e. fifth to eighth excited levels above the ground state) are not covered by our spectrum, being located bluewards of the observed wavelength range. The Mn II $\lambda\lambda\lambda2576,2594,2606$ triplet and Mn II* transition lines (i.e. $\lambda\lambda2933,2940,2950$) from the first excited level of Mn II, with an excitation energy of 9473 cm^{-1}, are detected most clearly in the *C* (reddest) and *A* (bluest) clumps (see Fig. A5). Such transitions were detected before only in a few FeLoBALs (e.g. FBQS J 1151+3822; Lucy et al. 2014).

Ca I $\lambda4227$ and CH$^+$ $\lambda\lambda3958,4233$ absorptions are not detected. Using the oscillator strengths of CH$^+$ lines from Weselak et al. (2009), we derive a 2σ upper limit on the column density of $N(CH^+) = 10^{13}$ cm^{-2} for each of the three complexes. We detect possible Na I emission lines in both the UVES and SDSS spectra. All absorption lines in the UVES spectrum were identified, except a weak line at $\lambda_{obs} = 5341$ Å, which has a similarly wide profile as the FeLoBAL lines. Searching an identification in the NIST data base at the different BAL sub-redshifts did not provide any satisfactory solution, therefore it has likely spurious nature.

3.3 Evidence of partial flux covering from Mg II

Singly ionized magnesium exhibits an overall similar velocity structure as Ca II, but much stronger lines, hence additional components are detected in the Mg II profiles. Since the Mg II lines are saturated (see Fig. 2), it would not be reasonable to fit such complex profiles as the velocity decomposition would be unreliable and solutions degenerate. However, we can obtain qualitative results by comparing the apparent optical-depth ratios of the Mg II doublet lines, τ_1/τ_2 (where τ_1 and τ_2 are the apparent optical depths in Mg II $\lambda2796$ and Mg II $\lambda2803$, respectively). This is shown in Fig. 3 for all three absorption-lines complexes, *A*, *B*, and *C*. When the absorber fully covers the continuum source, the apparent optical-depth ratio of the Mg II doublet is expected to be $\tau_1/\tau_2 = f_1\lambda_1/f_2\lambda_2 \approx 2$ (where f_i and λ_i are the line oscillator strengths and wavelengths, respectively), unless the lines are not fully saturated. One can see in Fig. 3 that in our case τ_1/τ_2 is close to unity along the entire profiles, which, together with *seemingly* saturated profiles, is evidence for partial flux covering. In the case of fully saturated line profiles, partial covering factors (C_f) can be roughly determined as $C_f \approx 1 - e^{-\tau_1}$. Therefore, a value of τ_1/τ_2 close to unity even in the line wings (where the optical depths $\tau_{1,2} < 1$) indicates that partial covering is likely changing through the profile, which may additionally complicate line-profile fitting. Using the flux residuals observed at the bottom of the profiles (where $\tau_1/\tau_2 \approx 1$), we derive upper limits on C_f of ∼0.82, 0.68, and 0.96, in complexes *A*, *B*, and *C*, respectively. We also note that the Mg II $\lambda\lambda2796$, 2803 lines are not blended with each other, with the exception of the far wings of Mg II $\lambda2803$ and Mg II $\lambda2796$ in complexes *A* and *B*, respectively. In addition, the velocity differences between complexes *A*, *B*, and *C*, and the weaker complex at $z \approx$ 0.3357 do not correspond to any of the strong high-ionization line-doublet splitting, i.e. Si IV, C IV, N V, nor O VI. Therefore, line locking (see e.g. Bowler et al. 2014) is not clearly present in this system.

---

[1]Based on Mg II lines this system does not satisfy standard BAL definition (Weymann, Carswell & Smith 1981), and should be attributed to the mini-BAL. However, C IV lines (that are typically used in BAL definition and usually indicate much wider profiles than Mg II lines) are out of the spectral range. Therefore, we will keep the denotation of this system as FeLoBAL, which is supported by the example of Q 2359−1241 (Arav et al. 2001), for which Mg II lines indicate a similar width as in J 1652+2650, but *HST* observations confirm large width of C IV lines.

[2]When selecting this quasar to search for intervening molecular absorption, we assumed the line of sight could intersect three galaxies (possibly located in a cluster hosting the quasar). It turns out that the gas is associated with the quasar active nucleus itself in spite of its low ionization.
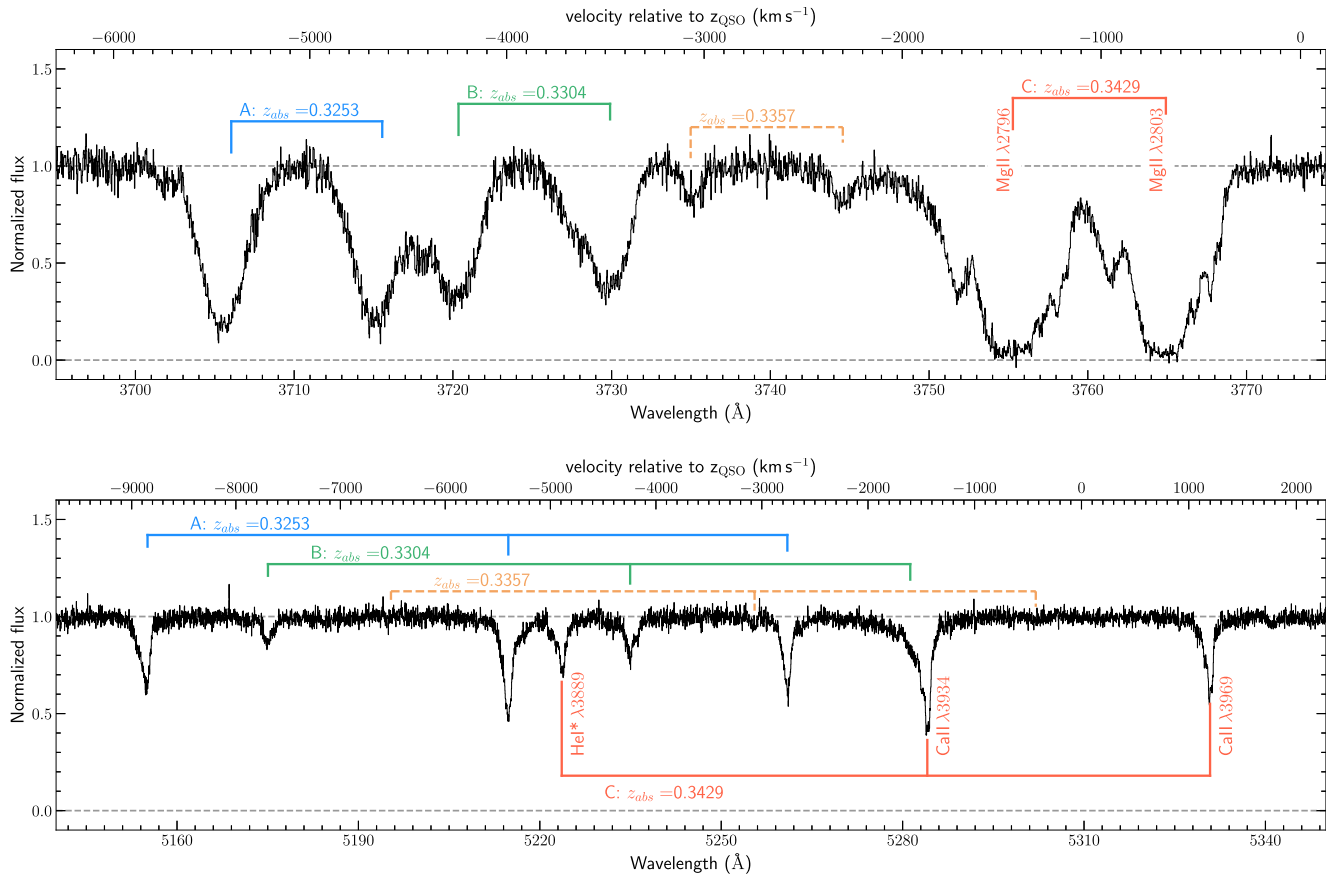
Figure 2. Portions of the normalized UVES spectrum showing the kinematics of Mg II (upper panel), Ca II H and K, and He I* λ3889 (lower panel) in the FeLoBAL towards J 1652+2650. The Mg II absorption-line complex at $z \approx 0.3357$ is much weaker than complexes *A*, *B*, and *C*, and therefore is not included in the following Voigt-profile fitting analysis. In both panels, the top axis shows the velocity of the strongest transition, i.e. Mg IIλ2796 (upper panel) or Ca IIλ3934 (lower panel), relative to the quasar systemic redshift.

## 3.4 Voigt-profile fitting of Ca II, Mg I, He I*, Fe II, and Mn II

We performed simultaneous fits to Ca II, Mg I, He I*, Fe II, and Mn II absorption lines using multiple-component Voigt profiles. While even Ca II λλ3934, 3969, Mg I λ2852, and He I* (λλλ2945, 3188, 3889) lines are located in spectral regions of high S/N, the weakness of some of the velocity components prevents us from fitting the lines individually. Additionally, Fe II and Mn II lines are significantly blended with each other, not only between components of a given complex (*A*, *B*, or *C*) but also between components pertaining to different complexes. Therefore, to obtain internally consistent fits, we tied the Doppler parameters in each component assuming them to be equal for each species. This implicitly assumes that turbulent broadening dominates over thermal broadening (micro-turbulence assumption), which is reasonable for the wide (FWHM > 15 km s^{-1}) profiles of this system.

As we mentioned, absorption lines from Fe II and Mn II in the UVES spectrum display a high degree of mutual blending and complexity; therefore, in order to remove possible degeneracies, we assumed that the Fe II levels are populated by collision with electrons (as argued for the majority of previously studied FeLoBALs (Korista et al. 2008; Bautista et al. 2010; Dunn et al. 2010; Byun et al. 2022a). This assumption also minimizes the number of independent variables in the analysis. Thus, for each velocity component, the column densities of Fe II levels are set by the total Fe II column density, the electron density, and the temperature. The data for the

strengths of collisions with electrons were taken from the CHIANTI 9.0.1 data base (Dere et al. 2019) and the atomic data from the NIST data base. We did not find any data for the collisional excitation of Mn II levels. Therefore, we could not consider its excitation together with Fe II and hence we derived the column densities of the Mn II and Mn II* levels, independently from Fe II. The atomic data for He I* and Ca II were taken from Drake & Morton (2007) and Safronova & Safronova (2011), respectively. For lines from excited levels of Fe II and Mn II, we used the data from Nave & Johansson (2013), Schnabel, Schultz-Johanning & Kock (2004), and Kling & Griesmann (2000), respectively. For other species, we used the atomic data compiled by Morton (2003).

Similar to the analysis of Mg II lines in Section 3.3, the apparent optical depth of the Ca II (as well as Fe II) lines indicates partial covering. Therefore, we need to include partial covering in the line-profile fitting procedure and for this we used the simple model proposed by Barlow & Sargent (1997; see also Balashev et al. 2011). Within this model, it is assumed that the velocity components with non-unity covering factors spatially overlap. If it were not the case, this would introduce additional covering factors to describe mutual overlapping (see e.g. the discussion in Ishita et al. 2021). When many components are intertwined in wavelength space, this requires a significant increase in the number of independent variables for the analysis (up to the factorial of *n*, where *n* is the total number of components). This complicates the analysis and makes the derived results ambiguous. Therefore, we made no attempt here to include
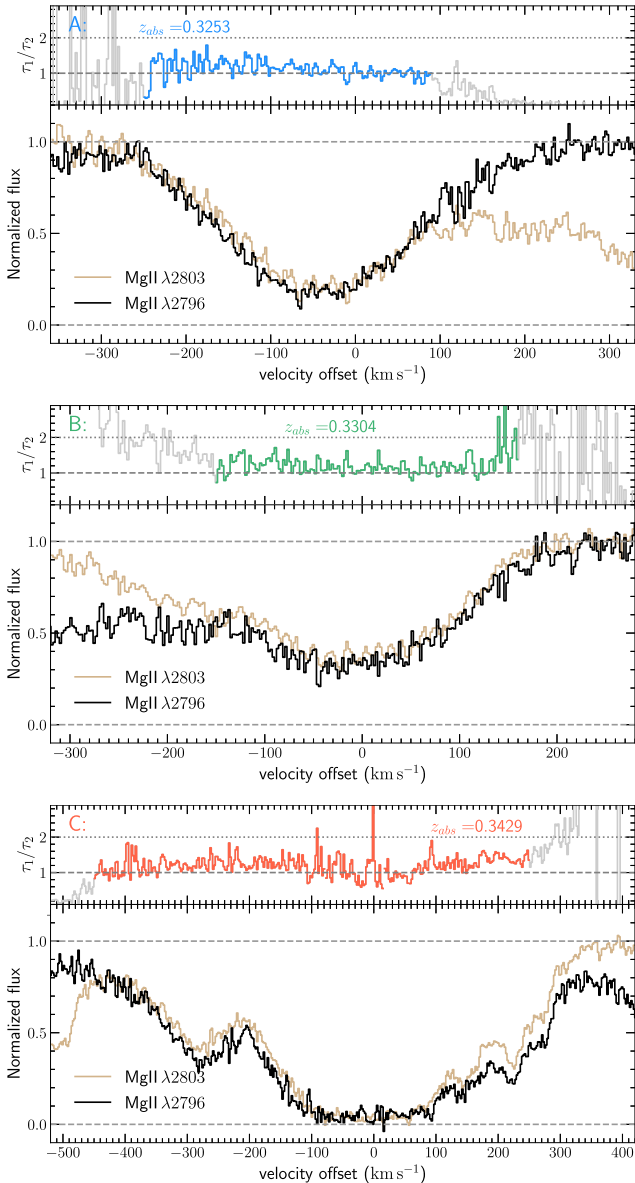
Figure 3. *Top to bottom*: Mg II in absorption-line complexes *A*, *B*, and *C*, at $z_{abs} = 0.32531$, 0.33043, and 0.34292, respectively. *Upper insets in each panel:* apparent optical-depth ratio of the Mg II doublet. The regions where the lines are not apparently blended are highlighted in colour (blue, green, or red). The dashed and dotted horizontal lines correspond to the ratio expected in the cases of complete line saturation ($\tau_1/\tau_2 = 1$) and optically thin lines ($\tau_1/\tau_2 = 2$), respectively.

mutual covering in the fitting procedure but rather tied the covering factors of all the components within the same complex (i.e. *A*, *B*, or *C*) to be the same. The model employed here therefore can only provide coarse estimates of the covering factors.

The likelihood function was constructed using visually identified regions of the spectrum that are associated with the lines to be fitted assuming a normal distribution of the pixel uncertainties. To obtain the posterior probability functions on the fit parameters (i.e. column densities, redshifts, Doppler parameters, and covering factors), we used a Bayesian approach with affine-invariant sampler (Goodman & Weare 2010). We used flat priors on redshifts, Doppler parameters, covering factors, and logarithms of column densities. For the electron temperature (which is relevant for lines from the excited Fe II levels),

we used a Gaussian prior of $\log T_e = 4.2 \pm 0.5$, corresponding to the typical electron temperatures of a fully ionized medium, where excited Fe II levels are highly populated (e.g. Korista et al. 2008). The sampling was performed on the cluster running ≈ 100 processes in parallel (using several hundred walkers) which typically took a few days until convergence. While this approach allows us to constrain the full shape of the posterior distribution function for each parameter, in the following text we report the fit results in a standard way. The point and interval estimates correspond to the maximum posterior probability and the 0.683 credible intervals obtained from 1D marginalized posterior distribution functions.

The results of Voigt-profile fitting are given in Table 1 and the modelled line profiles are briefly shown in Fig. 4, and fully displayed in Figs A1−A5. The derived Doppler parameters span a wide range, from several up to 200 km s^{-1}. The largest Doppler parameters found here should however be considered as upper limits only due to our inability to unambiguously resolve the line profiles in individual components owing to insufficient spectrum quality and few available transitions. While the column-density ratios between components are not drastically varied, some trends likely appear. For example, the components in complex *A* have a much larger Ca II-to-Mg I column-density ratio than the components in complexes *B* or *C*. This likely indicates that the physical conditions vary from one complex to the other. Alternatively, this may indicate that the species under study are not co-spatial, which would weaken the assumption of identical Doppler parameters and location in velocity space for the considered species. Therefore, the derived uncertainties on the column densities should be considered with caution as they only describe uncertainties in a statistical sense. In complexes *A*, *B*, and *C*, the covering factors,C_f, are measured to be $0.53^{+0.01}_{-0.01}$, $0.24^{+0.01}_{-0.01}$, and $0.81^{+0.01}_{-0.01}$, respectively, where again the quoted uncertainties should be considered with caution given the assumptions discussed above. The covering factors are mainly constrained by the Ca II and Fe II lines since the He I* and Mn II lines are weak (and hence are less sensitive to partial covering) and Mg I exhibits a single line. Therefore, the Mg I column densities reported in Table 1 are only reliable if the Mg I-bearing gas is co-spatial with Ca II. One should also note that the covering factors derived here are smaller than those found for Mg II in Section 3.3. This indicates that the spatial extent of the Mg II-bearing gas is larger than that of Ca II and Fe II.

In Fig. 5, we plot the physical parameters derived using the lines from excited levels of Fe II for velocity complexes *A*, *B*, and *C*. We found that the electron densities in different components lie in the range $n_e \approx [10^2; 10^5]$ cm^{-3}, which is expected given the detection of highly excited levels (with energies $\lesssim 10^4$ cm^{-1}). Interestingly, the electron densities in complex *A* are found to be systematically higher than in *B* or *C*. This suggests that complex *A* is located closer to the central engine in a harsher environment, which in turn is in agreement with the assumption that these complexes are produced in a decelerated-wind medium. We however note that the line profiles are quite complex and therefore exact velocity decomposition is quite complicated in this system and hence our solution is not necessary to be unique.

The electron temperature is found to be in the wide range $T_e \approx 10^{3.5}$–$10^{4.5}$ K, close to the observationally motivated chosen priors. This is not surprising since collisional population is less sensitive to the temperature than to the number density itself. Using the inferred electron densities (representing the number density, since the excited Fe II originates from ionized gas (see e.g. Korista et al. 2008), and the total column density of Fe II one can derive the longitudinal extent of the absorbing clouds associated with each component, which we found to also span a wide range. When inferring this value, one should

Table 1. Results of simultaneous fits (shown in Figs 4 and A1−A5) to absorption lines from Fe II, Ca II, He I*, Mg I, and Mn II in the FeLoBAL towards J 1652+2650.

Comp.	z	Δv^a [km s^{-1}]	b [km s^{-1}]	log n [cm^{-3}]	log T [K]	log N_{tot}(Fe II)	log N(Ca II)	log N(He I*)	log N(Mg I)	log N(Mn II)	log N(Mn II*)	C_f
A, 1	$0.324862(^{+23}_{-15})$	−5778	46^{+7}_{-5}	<2.9	>4.0	$13.44^{+0.23}_{-0.24}$	<10.6	$13.48^{+0.08}_{-0.04}$	<11.1	<11.3	<11.9	$0.531^{+0.012}_{-0.008}$
A, 2	$0.325195(^{+14}_{-20})$	−5704	$44.3^{+1.8}_{-2.4}$	$4.28^{+0.11}_{-0.08}$	$3.9^{+0.1}_{-0.1}$	$14.60^{+0.05}_{-0.07}$	$12.90^{+0.05}_{-0.08}$	$13.90^{+0.05}_{-0.05}$	$12.39^{+0.07}_{-0.05}$	$13.26^{+0.07}_{-0.08}$	$12.33^{+0.13}_{-0.14}$	'
A, 3	$0.3253310(^{+30}_{-30})$	−5674	$29.0^{+0.8}_{-1.2}$	>4.8	$3.7^{+0.1}_{-0.1}$	$14.27^{+0.10}_{-0.12}$	$13.18^{+0.04}_{-0.04}$	$13.59^{+0.10}_{-0.09}$	$12.29^{+0.06}_{-0.10}$	$13.04^{+0.10}_{-0.18}$	$12.57^{+0.06}_{-0.06}$	'
A, 4	$0.325432(^{+17}_{-17})$	−5651	181^{+3}_{-7}	$4.55^{+0.08}_{-0.07}$	$4.4^{+0.1}_{-0.2}$	$14.69^{+0.05}_{-0.03}$	$13.154^{+0.019}_{-0.011}$	$13.59^{+0.04}_{-0.04}$	$12.57^{+0.04}_{-0.04}$	$13.23^{+0.12}_{-0.14}$	$12.56^{+0.10}_{-0.21}$	'
B, 5	$0.329670(^{+30}_{-40})$	−4710	125^{+14}_{-9}	$3.7^{+0.3}_{-0.3}$	$3.9^{+0.3}_{-0.2}$	$14.91^{+0.10}_{-0.15}$	$12.97^{+0.04}_{-0.06}$	$13.55^{+0.07}_{-0.07}$	$12.83^{+0.05}_{-0.06}$	$13.29^{+0.10}_{-0.19}$	$12.89^{+0.10}_{-0.12}$	$0.235^{+0.011}_{-0.012}$
B, 6	$0.330355(^{+18}_{-21})$	−4559	27^{+4}_{-4}	<2.1	>3.9	$15.5^{+0.4}_{-0.5}$	$12.72^{+0.11}_{-0.15}$	$13.41^{+0.11}_{-0.16}$	<12.1	<12.9	$12.36^{+0.17}_{-0.23}$	'
B, 7	$0.330433(^{+12}_{-13})$	−4542	15^{+4}_{-4}	<4.6	$4.1^{+0.6}_{-0.3}$	<13.2	$12.39^{+0.18}_{-0.26}$	$12.9^{+0.3}_{-0.3}$	<12.4	$12.97^{+0.24}_{-0.32}$	<11.6	'
B, 8	$0.330513(^{+13}_{-17})$	−4524	72^{+4}_{-3}	$4.0^{+0.1}_{-0.2}$	$3.92^{+0.10}_{-0.03}$	$15.09^{+0.10}_{-0.09}$	$13.23^{+0.04}_{-0.05}$	$13.98^{+0.03}_{-0.07}$	$12.97^{+0.03}_{-0.08}$	$13.27^{+0.15}_{-0.20}$	$12.63^{+0.15}_{-0.25}$	'
C, 9	$0.341623(^{+30}_{-30})$	−2059	140^{+17}_{-29}	$4.8^{+0.6}_{-0.3}$	$3.9^{+0.2}_{-0.1}$	$14.09^{+0.05}_{-0.07}$	$12.30^{+0.05}_{-0.08}$	<12.7	$12.07^{+0.08}_{-0.06}$	<12.5	$12.35^{+0.09}_{-0.13}$	$0.807^{+0.010}_{-0.014}$
C, 10	$0.342551(^{+32}_{-28})$	−1853	62^{+6}_{-7}	$3.14^{+0.21}_{-0.17}$	$3.8^{+0.1}_{-0.1}$	$14.42^{+0.05}_{-0.06}$	$12.56^{+0.06}_{-0.06}$	$13.35^{+0.05}_{-0.07}$	$12.42^{+0.05}_{-0.08}$	$12.94^{+0.07}_{-0.10}$	<12	'
C, 11	$0.342705(^{+6}_{-15})$	−1819	$20.2^{+1.5}_{-3.2}$	$3.40^{+0.16}_{-0.11}$	$3.9^{+0.2}_{-0.1}$	$14.15^{+0.16}_{-0.11}$	$12.29^{+0.05}_{-0.14}$	$12.52^{+0.20}_{-0.18}$	$12.15^{+0.06}_{-0.14}$	$12.27^{+0.24}_{-0.38}$	<11	'
C, 12	$0.342821(^{+25}_{-15})$	−1793	14^{+11}_{-3}	$3.8^{+1.1}_{-0.3}$	$3.7^{+0.3}_{-0.3}$	$13.6^{+0.5}_{-0.4}$	$12.05^{+0.22}_{-0.21}$	<12.3	$11.93^{+0.25}_{-0.21}$	$12.59^{+0.28}_{-0.16}$	$11.84^{+0.14}_{-0.22}$	'
C, 13	$0.3428840(^{+30}_{-30})$	−1779	$8.9^{+1.3}_{-1.2}$	$3.7^{+0.5}_{-1.0}$	$3.7^{+0.2}_{-0.3}$	$13.67^{+0.18}_{-0.25}$	$12.25^{+0.11}_{-0.12}$	$12.42^{+0.22}_{-0.12}$	$12.06^{+0.09}_{-0.13}$	<12.1	<11.1	'
C, 14	$0.342930(^{+14}_{-14})$	−1769	25^{+4}_{-4}	$2.8^{+0.3}_{-0.6}$	$4.0^{+0.1}_{-0.1}$	$14.91^{+0.26}_{-0.15}$	$12.48^{+0.10}_{-0.19}$	$12.99^{+0.09}_{-0.16}$	<12.1	$13.03^{+0.11}_{-0.27}$	<11.6	'
C, 15	$0.342996(^{+4}_{-5})$	−1754	$14.2^{+1.1}_{-1.0}$	$3.6^{+0.6}_{-0.4}$	$3.7^{+0.3}_{-0.3}$	$13.74^{+0.23}_{-0.22}$	$12.39^{+0.09}_{-0.08}$	$12.75^{+0.12}_{-0.12}$	$12.34^{+0.05}_{-0.08}$	$12.60^{+0.18}_{-0.27}$	$11.81^{+0.16}_{-0.19}$	'
C, 16	$0.3430353(^{+59}_{-29})$	−1745	$68.6^{+3.2}_{-2.4}$	$4.18^{+0.05}_{-0.07}$	$4.0^{+0.1}_{-0.1}$	$14.54^{+0.04}_{-0.03}$	$12.67^{+0.02}_{-0.02}$	$13.55^{+0.03}_{-0.02}$	$12.27^{+0.05}_{-0.04}$	$12.88^{+0.09}_{-0.11}$	$12.15^{+0.14}_{-0.21}$	'
C, 17	$0.343601(^{+10}_{-7})$	−1620	19^{+4}_{-3}	$5.2^{+1.3}_{-1.0}$	$4.2^{+0.5}_{-0.3}$	$13.16^{+0.24}_{-0.22}$	$11.48^{+0.08}_{-0.10}$	$12.53^{+0.09}_{-0.10}$	<11.4	<11.9	<11.9	'
C, 18	$0.343902(^{+16}_{-20})$	−1553	47^{+8}_{-6}	$4.5^{+0.5}_{-0.4}$	$4.2^{+0.3}_{-0.5}$	$13.71^{+0.07}_{-0.13}$	$11.79^{+0.08}_{-0.04}$	$12.75^{+0.06}_{-0.09}$	$11.63^{+0.09}_{-0.09}$	<11.9	<11.9	'

Note.^{a} relative to $z_{sys} = 0.3509$ (as determined in Section 3.1).

take into account the Fe gas abundances. If we assume a solar Fe II abundance, we get characteristic values of about 10^{15} and $10^{15.5}$ cm for complexes A and B, respectively, and a wide range of values for complex C. These values should be considered as lower limits only, since neither the metallicity nor the Fe depletion, nor the Fe II ionization correction, are known. Indeed, the depletion of Fe is much less than <1 and a very sensitive function of metallicity, and Fe II can be a subdominant form of Fe, even where excited Fe II levels are populated (see e.g. Korista et al. 2008). The ratio of Mn II* to Mn II column densities was found to be around 0.1–0.3, similar to Fe II, where complex A exhibits slightly higher excitation than complex C (Mn II* is very unconstrained in complex B). If fitted individually, the covering factors derived here for each complex were found to be consistent between Ca II and Fe II, which indicates that Fe II- and Ca II-bearing clouds likely have similar spatial extents.

3.4.1 On the possibility of UV pumping

We tried to model the excitation of the observed Fe II levels by UV pumping instead of collisions with electrons since the UV flux can be very high for gas in the vicinity of the central engine. To do this, we used the data of transition probabilities from the NIST data base to calculate the excitation through UV pumping. We note that UV pumping can easily be incorporated into the fit only in the optically thin regime (corresponding to log N(Fe II) $\lesssim$ 13), which is not the case for most components. Therefore, a complex multiple-zone excitation model should be implemented that takes into account radiative transfer fully, since the UV excitation at some position depends on the line profiles, and therefore on the excitation balance at the regions closer to the radiation source. This implementation however is impractical for such a complex line-profile fitting as we have towards J 1652+2650. However, we can draw qualitative conclusions from the following two limiting cases: the optically thin limit, or assuming constant dilution of the excitation using typically observed column densities.

In the optically thin case, we found that UV pumping does not provide satisfactory fits, since it cannot reproduce the observed excitation of the Fe II levels as well as collisional excitation can do. To qualitatively illustrate this, we plot in Fig. 6 the excitation of Fe II levels as a function of electron density and UV field. The UV field is expressed in terms of distance to the central engine estimated from the observed r-band J 1652+2650 magnitude of 17.0 assuming a typical quasar spectral shape. One can see that the Fe II excitation described by typically estimated electron densities (for example, at $n_e \approx 10^4$ cm^{-3}, which are shown by a dashed line in each panel of Fig. 6), corresponds to roughly a factor of 2 difference in distance (hence a factor of 4 difference in UV flux) that is needed to describe the fine-structure levels of the ground term (3d^{6}4s ^{6}D, representing excited levels from first to fourth) and the second excited (3d^{6}4s ^{4}D, representing excited levels from 9th to 12th) Fe II term. From this diagram, one can see that if the excitation is described by UV pumping the absorbing gas must be located a few tens of parsec away from the central engine. However, if UV pumping dominates the excitation of the Fe II levels, this results in very large values of the ionization parameter, log $U \gtrsim -1$, that is difficult to reconcile with the survival of Fe II and other associated low-ionization species (e.g. Ca II and Na I). Additionally, the observed column density of He I* indicates log $U \approx -3$ for dense gas, which is discussed later in Section 4. All this indicates that UV pumping is unlikely to be the dominant excitation process at play in the gas. Using calculations in the optically thick regime and assuming log N(Fe II) = 14 we found less disagreement in the UV fluxes required to populate the low and high Fe II levels. However, the optically thick case implies smaller distances to the central engine and hence even higher ionization parameters, in comparison to the optically thin case.

4 PHOTOIONIZATION MODEL

We modelled the abundance of He I* to estimate the physical conditions of the gas associated with this small-detached narrow/low-ionization BAL towards J 1652+2650. As discussed by, e.g. Arav
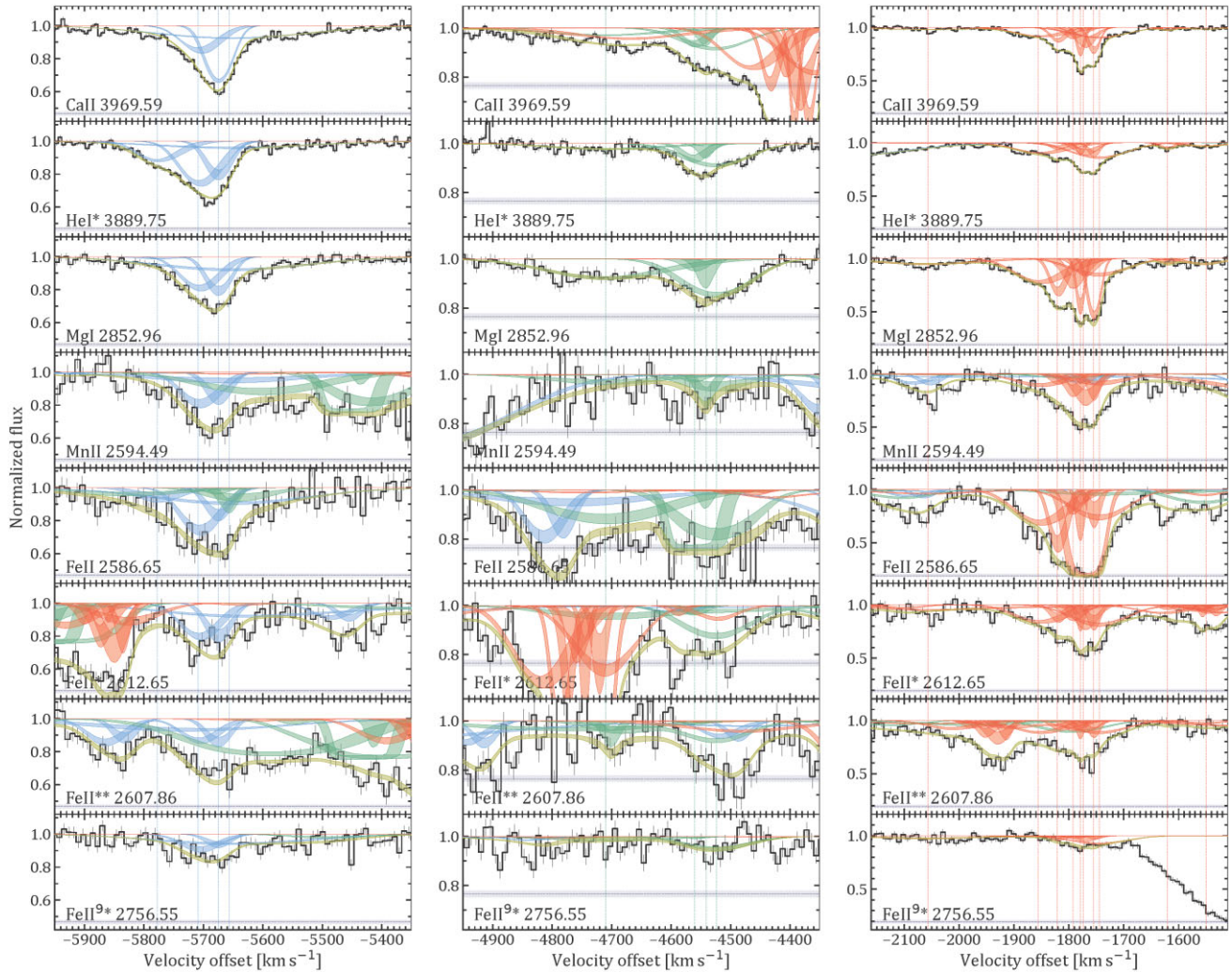
Figure 4. *Left to right*: Voigt-profile fits to selected Ca II, He I⋆, Mg I, Mn II, and Fe II absorption lines in complexes *A* (left), *B* (middle), and *C* (right), at z_{abs} = 0.3253, 0.3304, and 0.3429, respectively, towards J 1652+2650. The coloured stripes show a 0.683 credible interval of the line profiles sampled from posterior probability distributions of fitting parameters. The yellow represents the total line profile, while the blue, green, and red lines indicate individual components from complexes *A*, *B*, and *C*, respectively. The vertical lines show the positions of each component. The horizontal dashed lines and their surrounding grey areas indicate the extent of partial covering determined by fitting each clump independently with its own covering factor. The spectrum was rebinned to 0.1 Å scale for presentation purposes. Note the different *y*-axis scaling in each column. The original spectrum and all absorption-line profiles are displayed in Figs A1−A5.

et al. (2001) and Korista et al. (2008), the meta-stable $2\,^3S$ level of He I⋆ is mostly populated through He II recombination and depopulated by radiative transition and collisional de-excitation. Therefore, He I⋆ predominantly originates from a layer of ionized gas where helium is in the form of He II and $n_e \approx n_H$, and the He I⋆ column density is sensitive to the number density and ionizing flux. In that sense, He I⋆ is an exceptional diagnostic of the physical conditions, almost independent of metallicity and depletion, unlike other metals. This is particularly relevant for the FeLoBAL under study since we can measure neither the abundance of H I nor the total abundance of any metal (i.e. only the singly ionized state of each species is constrained), hence we have neither a measurement of metallicity nor metal depletion in this system. This limitation is also an issue for most of the previously studied FeLoBAL systems, and the assumption of a particular metallicity value can significantly affect the physical conditions derived from the photoionization modelling (e.g. Byun et al. 2022b).

We used the latest public version of the CLOUDY software package C17.02 (Ferland et al. 2017) to model a slab of gas in the vicinity

of the AGN. Our basic set-up is a cloud of constant density that is illuminated on one side by a strong UV field with a typical AGN spectrum. We assumed a metallicity of 0.3 solar,[3] a characteristic value for such clouds, but we also checked that the exact metallicity value has little impact on the derived He I⋆ column densities. Temperature balance was calculated self-consistently. As a stopping criterion, we used a total Fe II column density of $10^{15}\ cm^{-2}$ corresponding to the higher end of Fe II column densities observed within the FeLoBAL components.

We ran a grid of photoionization models by varying two main parameters: the number density and the ionization parameter, within the ranges of log [1; 6] and log [−4; 0], respectively. Fig. 7 shows the

---

[3]We took solar relative abundances of the metals, i.e. we did not use any depletion factor. While in the most known FeLoBALs the metallicity is found to be around solar value (e.g. Arav et al. 2001; Aoki et al. 2011; Byun et al. 2022b), our chosen value 0.3 mimics possible Fe depletion, which is typically large (up to 2 dex) at solar metallicity.
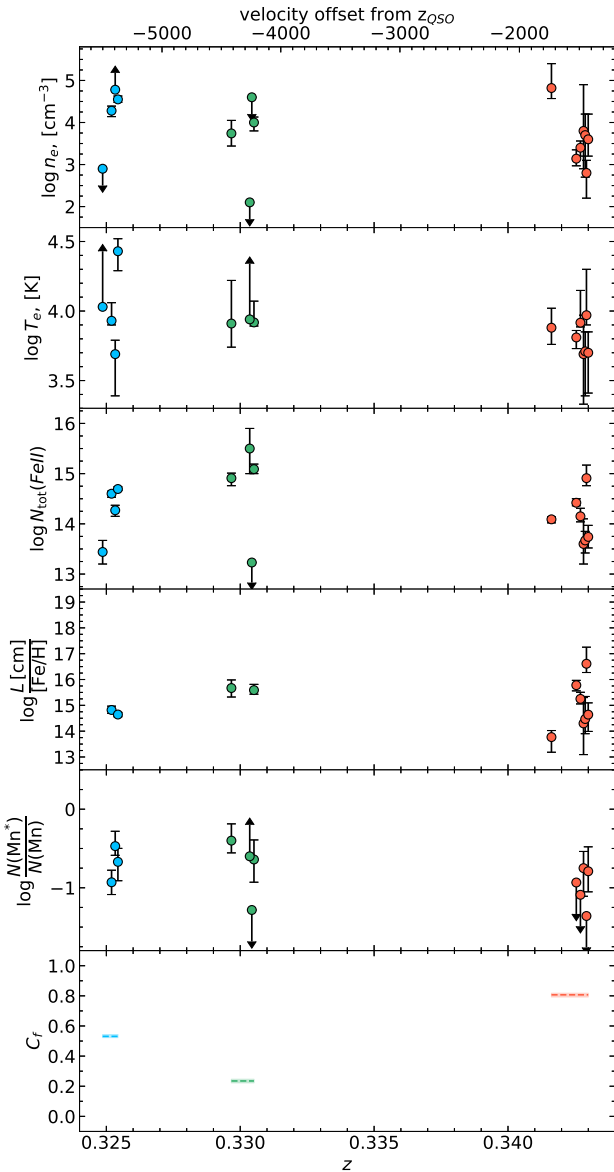
Figure 5. Comparison of physical parameters in velocity complexes *A*, *B*, and *C* (in blue, green, and red, respectively) towards J 1652+2650. The values are taken from Table 1, except [Fe/H], which is the Fe gas-phase abundance relative to the solar. For presentation purposes, we only show the values that are reasonably well-constrained. In the lower panel, larger values of C_f correspond to larger covering factors.

constraints on each parameter derived from the comparison of the modelled He I* column density with the fiducial value of 13.7 ± 0.1, typical of high column-density components. One can see that the modelling provides estimates on the number of ionizing photons of $\log(U n_{\rm H}) \approx 0.5$ for $\log n_{\rm H} \lesssim 4$, and $\log U \approx -3$ for $\log n_{\rm H} \gtrsim 4$. The latter solution to preferred value by the excitation of Fe II, which provides an independent constraint on $\log n_{\rm H} \approx 4$. Since the excited Fe II levels predominately arise from the ionized medium (as they are excited by collision with electrons; see also Korista et al. 2008), this suggests that $n_{\rm e} \approx n_{\rm H}$ and hence likely, the He I* abundance provides an estimate of $\log U \sim -3$. While the exact value of $\log U$ for each component depends on the observed He I* column density, we refrain from using the latter because with such a modelling we

cannot be confident regarding constrained Fe II column densities, as mutual covering may impact the derived column densities. We also checked that the CLOUDY modelling roughly reproduces the Ca II, Mg I, and Mn II column densities. However, as we mentioned above, using the abundance of these species is limited due to unconstrained total metallicities and depletion patterns.

5 DISCUSSION

5.1 Case of FeLoBAL towards Q 2359−1241

One of the most comprehensive studies so far of a FeLoBAL by means of high-resolution spectroscopy concerns Q 2359−1241 (Arav et al. 2001). A broad and deep VLT/UVES spectrum of this quasar allowed Arav et al. (2008) to detect Fe II lines up to the eighth excited level (excitation energy of 7955 cm^{-1}) above the ground state, and to constrain the physical conditions in the associated medium (Korista et al. 2008). A sophisticated fitting model was used, describing partial covering of the source by the absorbing clouds based on a power-law distribution (see Arav et al. 2008). In this study, we used a model of uniform partial covering instead, which is dictated by the observation of complex mutually blended absorption-line profiles. In the case of Q 2359−1241, the line velocity structure is simpler, with only a few visually distinct velocity components, and the lines are not significantly saturated. This allows one to independently constrain the column density in each Fe II level and for each component, and then describe the population of Fe II levels to constrain the excitation mechanisms. Additionally, due to its higher redshift, the FeLoBAL towards Q 2359−1241 allows one to constrain the column density of intermediate Fe II levels with energies between 1872–3117 cm^{-1} (corresponding to the a^{4}F term of the 3d^7 configuration). We found that these levels are important to disentangle between radiative pumping and collisions with electrons. Certainly, such an independent determination of Fe II column densities is more robust than tightening them assuming a dominant excitation mechanism, as we did for J 1652+2650. Therefore, we endeavoured to test our procedure by also fitting the FeLoBAL towards Q 2359−1241 using the spectrum taken from the SQUAD data base (Murphy et al. 2019).

To fit the Fe II lines, we used an eight-component fit, out of which four components exhibit higher excitation and are mutually blended, and four components show a low level of excitation with only the first few excited levels above the ground state detected Bautista et al. (2010). We used the same Doppler parameters for all of the Fe II levels in a given component. We added an independent covering factor to each component, yet tying the covering factor to be equal in two closely associated weak components at $z = 0.8611$. The quasar continuum was re-constructed locally by interpolating the spectrum free from absorption features. We note that the continuum placement may be important for weak lines since the line profiles are fairly broad. The line-fitting procedure we used is the same as described for J 1652+2650 (see Sections 3.4). The fitting results are listed in Table 2 and the modelled line profiles are shown in the Appendix, in Figs A6 to A10. In comparison to the study of Arav et al. (2008) and Korista et al. (2008), we were able to identify a larger number of Fe II levels, up to the 12th excited level of Fe II (excitation energy of ∼8850 cm^{-1}) above the ground state.

We used the measured population of the Fe II levels to constrain the physical conditions in the absorbing medium. We used the same model as for J 1652+2650, where we considered the competition between collisions (with electrons) and radiative excitation (by UV pumping). In Figs 8 and 9, we show the excitation diagrams of
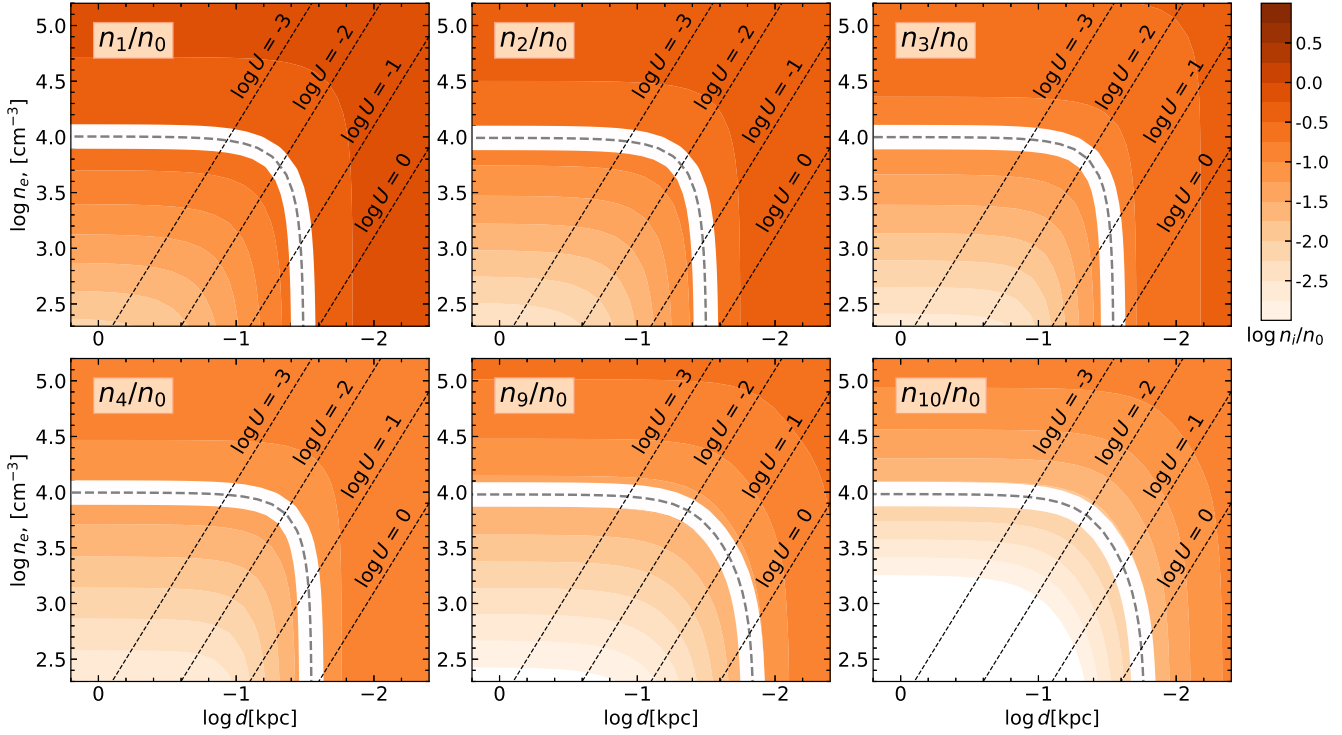
Figure 6. Excitation of Fe II levels as a function of electron density, n_e, and distance to the central engine, d. The latter is calculated from the measured photometric flux of J 1652+2650 assuming a typical quasar spectral shape. Calculations were performed in the optically thin limit, hence any constraint on the distance that can be obtained if UV pumping dominates the Fe II excitation must be considered as an upper limit. Additionally, we plot lines of constant ionizing parameter, U, calculated by scaling the UV flux and assuming bluewards of the Lyman limit an AGN spectrum with power-law shape with index -1.2. One can see that, for UV pumping to dominate the excitation of Fe II levels, the ionizing parameter must be larger than 0.01.
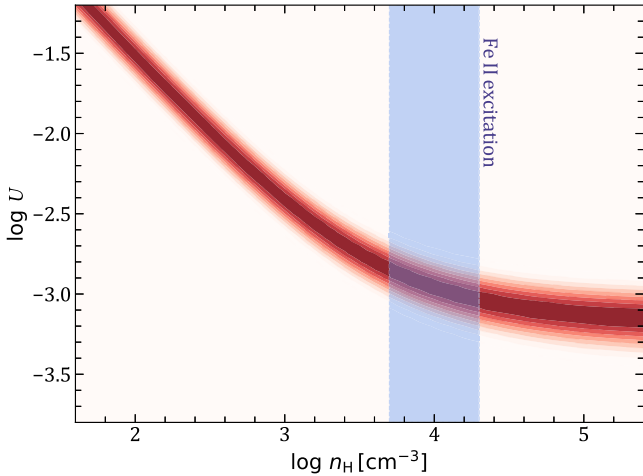
Figure 7. Constraints on the ionization parameter and number density from CLOUDY photoionization modelling of He I* in the FeLoBAL towards J 1652+2650. The region displayed in brown shows the estimated probability density function constructed by comparing the calculated He I* column densities with the observed typical value of $\log N = 13.7 \pm 0.1$ (see Table 1). The region displayed in blue shows the range of n_H values favoured by the measured Fe II excitation.

the different Fe II levels together with the constrained region of the parameter space of physical conditions, i.e. electron density, n_e, and UV field strength. As in Section 3.4.1, the UV field is expressed in terms of distance to the central engine as estimated from the r-

band Q 2359−1241 magnitude of ∼17.0 assuming a typical quasar spectral shape (Selsing et al. 2016). The 2D posterior parameter distributions were obtained using the likelihood function assumed to be a product of individual likelihoods of the comparison between the modelled and measured Fe II^{i*}/Fe II ratios.[4] We also assumed flat priors on $\log n_e$ and $\log d$ emulating a wide prior distribution for these two parameters. In Figs 8 and 9, one can see that in the components that have a large enough number of measured Fe II levels, the excitation is better reproduced by the model of collisions with electrons only, and therefore these components provide robust constraints on the electron density. For the components at $\Delta v = -1325$, -1299, and -1298 km s^{-1}, we found n_e to be in the range between 5×10^3 and 3×10^4 cm^{-3}. For the other components, the constrained posterior does not indicate a preferable source of excitation leaving the physical conditions poorly constrained over a wide range. However, for the weaker and most-redshifted components at $\Delta v > -1200$ km s^{-1}, the excitation of the Fe II levels is less and if it were dominated by collisions this would result in a significantly lower electron density, $\log n_e \sim 3.5$, than for the main components. In the three bluest components, where n_e is robustly measured, we can get an upper limit on the ionization parameter which was found to be $\log U \lesssim -3$, -1.5, and -2.5 for the components at $\Delta v = -1325$, -1299, and -1298 km s^{-1}, respectively. These

---

[4]The latter ratios were obtained directly from the fitting procedure. During the fit of the Fe II lines, the column densities of the different energy levels of Fe II were fitting parameters. However, since we used the MCMC method to sample the posterior distributions, we could simply obtain the posterior distributions for the aforementioned ratios.

Table 2. Results of simultaneous fits to absorption lines from Fe II ground state and excited levels in the FeLoBAL towards Q 2359−1241.

Comp.	#1	#2	#3	#4	#5	#6	#7	#8
z_{abs}	$0.859761(^{+10}_{-16})$	$0.859922(^{+7}_{-7})$	$0.8599318(^{+14}_{-9})$	$0.860189(^{+6}_{-5})$	$0.861056(^{+11}_{-6})$	$0.861127(^{+26}_{-15})$	$0.8618265(^{+17}_{-7})$	$0.8626427(^{+13}_{-10})$
Δv^a [km s^{-1}]	−1325	−1299	−1298	−1256	−1117	−1105	−992	−861
b [km s^{-1}]	$85.3^{+3.4}_{-1.9}$	$47.5^{+2.0}_{-1.8}$	$13.5^{+0.3}_{-0.3}$	$15.9^{+1.0}_{-1.2}$	$7.5^{+3.2}_{-1.5}$	$20.1^{+2.5}_{-3.1}$	$5.7^{+0.4}_{-0.4}$	$7.5^{+0.3}_{-0.3}$
log N(Fe II,g.s.)	$15.39^{+0.12}_{-0.06}$	$14.39^{+0.07}_{-0.04}$	$13.63^{+0.03}_{-0.03}$	$13.40^{+0.09}_{-0.17}$	$13.45^{+0.18}_{-0.18}$	$13.58^{+0.13}_{-0.17}$	$13.01^{+0.07}_{-0.10}$	$13.24^{+0.05}_{-0.04}$
log N(Fe II,j1)	$14.76^{+0.06}_{-0.07}$	$13.91^{+0.07}_{-0.05}$	$13.21^{+0.04}_{-0.04}$	$13.01^{+0.13}_{-0.15}$	$12.53^{+0.17}_{-0.25}$	$12.56^{+0.26}_{-0.55}$	$12.01^{+0.12}_{-0.12}$	$12.48^{+0.03}_{-0.06}$
log N(Fe II,j2)	$14.50^{+0.06}_{-0.07}$	$13.78^{+0.06}_{-0.09}$	$13.10^{+0.04}_{-0.04}$	$12.81^{+0.14}_{-0.13}$	$12.63^{+0.12}_{-0.29}$	$12.60^{+0.25}_{-0.58}$	$11.68^{+0.27}_{-0.39}$	$12.12^{+0.09}_{-0.09}$
log N(Fe II,j3)	$14.64^{+0.05}_{-0.08}$	$13.43^{+0.10}_{-0.05}$	$12.97^{+0.04}_{-0.03}$	$12.73^{+0.10}_{-0.13}$	$12.40^{+0.21}_{-0.42}$	$12.48^{+0.21}_{-0.96}$	$11.55^{+0.26}_{-0.33}$	$12.20^{+0.06}_{-0.09}$
log N(Fe II,j4)	$14.25^{+0.06}_{-0.08}$	$13.13^{+0.13}_{-0.14}$	$12.67^{+0.07}_{-0.03}$	<12.5	<12.2	<12.1	<11.7	<11.5
log N(Fe II,j5)	$15.33^{+0.10}_{-0.08}$	$14.26^{+0.10}_{-0.08}$	$13.70^{+0.05}_{-0.04}$	$13.22^{+0.32}_{-0.83}$	<13.5	<13.7	$12.64^{+0.19}_{-0.30}$	<12.6
log N(Fe II,j6)	$14.92^{+0.09}_{-0.09}$	<13.5	$13.29^{+0.07}_{-0.09}$	<13.0	–	–	–	–
log N(Fe II,j7)	$14.63^{+0.20}_{-0.16}$	$13.93^{+0.19}_{-0.31}$	<13.1	<12.8	–	–	–	–
log N(Fe II,j8)	$14.88^{+0.08}_{-0.11}$	<12.80	<13.0	<12.2	–	–	–	–
log N(Fe II,j9)	$14.02^{+0.12}_{-0.08}$	<12.8	$12.55^{+0.05}_{-0.05}$	$12.51^{+0.20}_{-0.30}$	–	–	–	–
log N(Fe II,j10)	$14.20^{+0.08}_{-0.06}$	$12.99^{+0.16}_{-0.12}$	$12.16^{+0.09}_{-0.12}$	<11.8	–	–	–	–
log N(Fe II,j11)	$13.75^{+0.12}_{-0.15}$	<12.2	$12.00^{+0.09}_{-0.15}$	<11.3	–	–	–	–
log N(Fe II,j12)	$13.46^{+0.09}_{-0.11}$	<12.3	$11.50^{+0.24}_{-0.54}$	$12.87^{+0.30}_{-0.44}$	–	–	–	–
log N_{tot}	$15.95^{+0.04}_{-0.04}$	$14.86^{+0.05}_{-0.04}$	$14.23^{+0.03}_{-0.04}$	$13.80^{+0.12}_{-0.14}$	$13.58^{+0.22}_{-0.15}$	$13.83^{+0.12}_{-0.21}$	$13.20^{+0.08}_{-0.10}$	$13.39^{+0.05}_{-0.05}$
C_f	$0.050^{+0.002}_{-0.005}$	$0.13^{+0.01}_{-0.01}$	$0.36^{+0.01}_{-0.02}$	$0.14^{+0.03}_{-0.03}$	$0.11^{+0.01}_{-0.01}$	$0.11^{+0.01}_{-0.01}$	$0.32^{+0.04}_{-0.04}$	$0.31^{+0.02}_{-0.02}$

Note.^{a} relative to $z_{sys} = 0.868$ (as reported by Brotherton et al. 2001).

values are reasonably consistent with the constraint of log $U \sim -2.4$ obtained from photoionization modelling of this system by Korista et al. (2008). It is also in line with the characteristic values we obtained in Sections 3 and 4 in the case of the FeLoBAL towards J 1652+2650.

In comparison with Korista et al. (2008) and Bautista et al. (2010), we derived significantly higher column densities for Fe II levels in all components (except at −992 km s^{-1}) and total column density as well, which is dominated by the velocity components at −1325 and −1299 km s^{-1}. This discrepancy is explained by the small covering factors of these two components, which allow the lines to be significantly saturated. However, the relative excitation of the Fe II levels even in these saturated components remains similar. Furthermore, the two central (in terms of apparent optical depth) components at −1298 and −1256 km s^{-1} indicate an excitation structure consistent with the results of Korista et al. (2008). We note that determining the exact profile decomposition is not trivial in such systems. We attempted to increase the number of fitted velocity components in Fe II lines but obtained more or less similar results, as additional components turned out to be weak if any. Moreover, the systematic uncertainty is most likely dominated by our choice of partial covering model, which is uniform with no mutual intersection (see Section 3.4). In terms of number density, we obtained similar results as Korista et al. (2008) who reported that log $n_H \sim 4.4 \pm 0.1$ considering total Fe II column densities only and a smaller number of energy levels than we do.

Overall, our approach (multicomponent model with a uniform covering factor) provides well-consistent results with those from earlier works, especially for derived physical quantity. While FeLoBALs in most cases are quite complicated for spectral analysis, such systems as one towards Q 2359−1241 provide an important example and testbed for the assumptions (e.g. collisionally dominated excitation) that can ease the analysis of more complex objects.

5.2 Similarities and differences between FeLoBALs

Previous studies indicate a wide range of physical conditions in FeLoBALs (and other intrinsic Fe II absorbers) with some kind of bimodal distribution, where part of the population is located at mild distances of ∼0.1–10 kpc and has number densities of <10^5 cm^{-3}, while the second part shows more extreme properties with number densities >10^8 cm^{-3} and distances to the nuclei down to ∼1 pc. This may be in line with state-of-the-art models of AGN outflows formation (Faucher-Giguère & Quataert 2012; Costa, Pakmor & Springel 2020), where the wind is a complex phenomenon that is driven by different mechanisms at different scales. It can be launched in the close vicinity of the accretion disc by radiative pressure and at a much larger distance by shocks, produced either by a wind from the accretion disc or the jet (e.g. Proga, Stone & Kallman 2000; Costa et al. 2020).

On the other hand, we note that ionization parameters around −1..−3 have been found for almost all detected FeLoBALs, while one would expect a wider range of values. This can be a selection effect, where such values of the ionization parameter are favourable for FeLoBAL observation. However, since $U \propto n^{-1}d^{-2}$ the observed bimodality can be an artefact of improper constraints on the physical conditions from the modelling. Indeed, the modelling of FeLoBALs is quite complex and ambiguous, and there are many factors that cannot be resolved using line-of-sight observations. FeLoBALs always exhibit a multicomponent structure, which makes the derivation of the physical conditions a difficult task, since several solutions are possible. A typical question arising from the photoionization modelling set-up is what is the relative position in physical space of the 'gaseous clouds' associated with each component? This impacts both the column density estimation, due to unknown mutual partial covering, and ionization properties, since the closest to AGN clouds will shield the farthest located ones. A relevant example of this situation is the FeLoBAL towards J 104459.6+365605, where Fe II excitation and simplistic photoionization modelling suggest
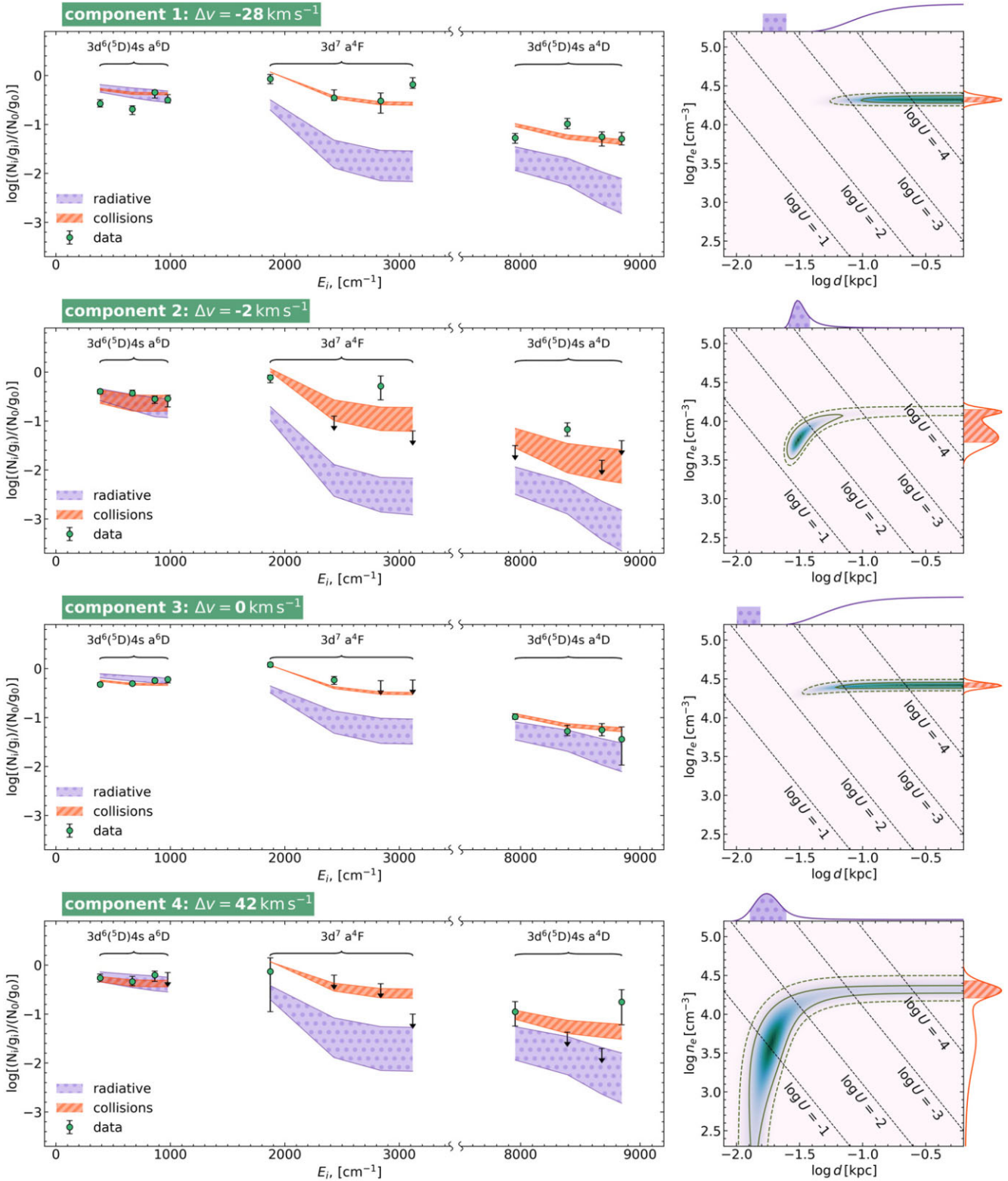
Figure 8. *Left panels:* Excitation diagrams of Fe II levels in the FeLoBAL towards Q 2359−1241. The *y*-axes indicate the ratio of the measured column density divided by statistical weight of i-th level to the ground level, while the *x*-axes provide the energy of the levels. The text in the upper part of each panel indicates the level terms. Each panel corresponds to a given velocity component as indicated in a green box on top of the panel. *Right panels:* Constrained physical conditions using the excitation of the Fe II levels shown in the left panels. The solid and dashed lines correspond to the 1σ and 2σ confidence intervals of the 2D posterior probability function, respectively. The violet and red curves on the top *x*-axis and right *y*-axis, respectively, show the 1D marginalized probability functions. The red and violet hatched regions below them indicate the approximate solutions where the population of the levels is dominated by collisions or radiative excitation, respectively. For illustrative purposes, the corresponding regions of the excitation diagrams are shown in the left panels using the same colours and hatch code.
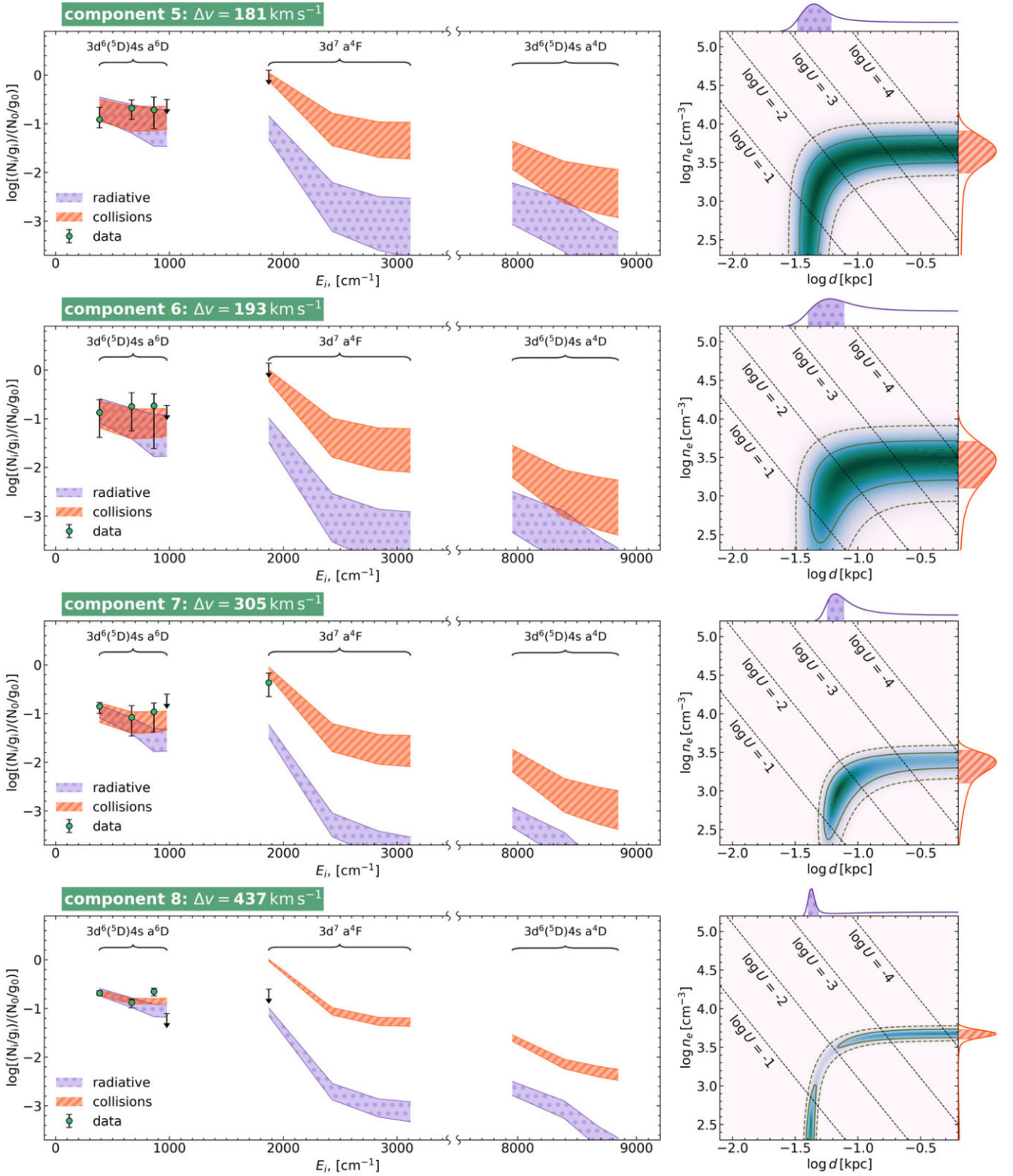
Figure 9. Continuation of Fig. 8.

relatively low number densities, $\log n_e < 4$, and a distance of $\sim$700 pc, while more sophisticated wind models (Everett, Königl & Arav 2002), which take shielding effects into account, yield number densities 10^4 times higher, and a distance of $\sim$4 pc. We note however that in the latter model, the excitation of Fe II levels is expected to be much higher than what is observed. In that sense, the usage of the excited fine-structure levels and He I* may provide less degenerated constraints than the relative abundances of the ions, the latter is also suffering from complications due to the unknown metallicity and depletion pattern (see discussion in Section 4).

5.3 Relation between FeLoBALs and other intrinsic absorbers

It is worth mentioning that a recently identified class of associated quasar absorbers bearing H_2 molecules exhibits distances to the AGN of $\sim$1–10 kpc (Noterdaeme et al. 2019, 2021, 2023), slightly higher, but comparable to what is derived for FeLoBALs. Interestingly, while the medium in such systems is neutral (and even at the H_I-H_2 transition), in contrast with FeLoBALs which arise in the ionized phase or at the boundary of the ionization front (e.g. Korista et al. 2008), they exhibit number densities of $\gtrsim 10^4$ cm^{-3}, similar to FeLoBALs. In the case of H_2-bearing systems, such number densities are required for H_2 to survive in the vicinity of the AGN (Noterdaeme et al. 2019) as the radiation fields are greatly enhanced. While in the case of J 1652+2650 we were not able to get constraints on the H_2 column density since the lines are out of the range of the spectrum, there is no H_2 detection in other FeLoBAL so far. Additionally, presented CLOUDY modelling (given in Section 4) suggests that the column densities and ionization parameter are not enough in FeLoBAL towards J 1652+2650 to expect the presence of the H_2 in such kind of medium.

Therefore, the difference between FeLoBALs and H_2-bearing systems may be related to the lower ionization parameters of the latter (akin to higher lower incident UV flux, or to their larger distances), which makes it possible for H_2 to survive or imply reasonable time-scales to form H_2. To elaborate on this we ran a grid of CLOUDY models to see how the conditions for the presence of H_2 and excited Fe II levels compared in the physical parameter space. We considered an isobaric model of the medium with 0.3 metallicity relative to solar (we additionally scaled the Fe abundance by 0.3 to emulate typical depletion at such metallicity) exposed by the AGN-shaped radiation field and regular cosmic ray ionization rate, 2×10^{-16} s^{-1} (for atomic hydrogen). We varied the ionization parameter and thermal pressure in ranges $\log U = -6..0$ (with 0.2 dex step) and $P_{th} = 10^5..10^{10}$ [K cm^{-3}] (with 0.5 dex step), respectively. We stopped the calculations either when the total H_2 or Fe II column densities reached characteristic values of $\log N(H_2) = 20$ or $\log N(Fe II) = 15$, respectively. The obtained contours of Fe II excitation and the total H_2 column density are shown in Fig. 10.

One can see that indeed, large H_2 column densities are found mostly outside the region of the parameter space where Fe II is highly excited, i.e. $\log Fe II^*/Fe II > -1$ (which is typical for the observed FeLoBAL systems), except only for the very high thermal pressures, $P_{th} \gtrsim 10^9$ K cm^{-3} and low ionization parameters $\log U \lesssim -4$. The presence of H_2 is mostly limited by the distances to the AGN, which in the case of J 1652+2650 corresponds to the values of several hundreds of pc.[5] In turn, the values measured Fe II*/Fe II coupled with the constrained ionization parameter $\log U \sim -3$ points to a low molecular fraction. We note that this modelling is indicative only, and one needs to be careful when comparing the measured excitation of the Fe II levels with the modelled one in this simulation. Indeed, in this particular modelling case, we stopped at a relatively large total Fe II column density, at which we may include a significant part of the neutral medium, where Fe II excitation is not so high as in the ionized shell.

The region in (U, P_{th}) parameter space where H_2 is present in copious amount is adjacent to the region where Fe II is reasonably excited (e.g. $\log N(Fe II^*)/N(Fe II) > -1$). That indicate that we may
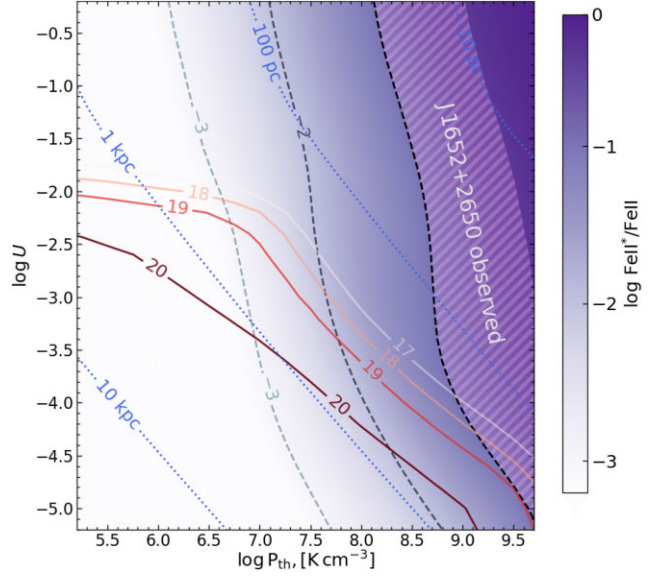
Figure 10. Constraints on the ionization parameter and thermal pressure from a grid of CLOUDY photoionization models (for set-up, see the text). The violet colour gradient and dashed contours show the excitation of Fe II, defined as $\log N(Fe II^*)/N(Fe II)$. The characteristic range of Fe II excitation observed in J 1652+2650 is shown by the hatched region. The red solid contours indicate the total H_2 column density, marked by values of $\log N(H_2)$. The blue dotted contours show the distance to the central engine calculated using the parameters of J 1652+2650.

witness the appearance of a global natural sequence among associated absorbers. The behaviour of this sequence is probably coupled with hydrodynamics processes in the outflowing gas, which set the thermal pressures and the sizes of the clumps and their dependence on the distance. Likely, a part of this sequence was observationally noticed by Fathivavsari (2020), regarding Coronographic (Finley et al. 2013) and Ghostly (Fathivavsari et al. 2017) DLAs, which also exhibit high excitation of fine-structure levels,[6] but that do not show Fe II*. The physical connection between these different classes of absorbers seems to be evident, with FeLoBALs representing predominantly gas at the ionization front, Coronographic and Ghostly DLAs being pre-dominantly neutral, and associated H_2-bearing absorbers tracing the H_I-to-H_2 transition. Importantly, both the ionization and photodissociation fronts are controlled by the ratio of UV flux to number density, i.e. the ionization parameter, while the appearance of a certain class of absorber also depends on the ambient thermal pressure and the total column density of the medium. In that sense, it will be important to observe and study systems of intermediate classes, displaying mixed properties. The search for such rare systems will be supported by the upcoming next-generation wide-field spectroscopic surveys such as 4MOST (Krogager et al. 2023), DESI (Chaussidon et al. 2023), and WEAVE (Jin et al. 2023).

6 SUMMARY

In this paper, we presented an analysis of the serendipitously identified FeLoBAL system at $z = 0.3509$ towards J 1652+2650 performed using a high-resolution UVES spectrum. The main aim

---

[5]Only a stationary cloud is considered here, i.e. we do not take into account the time-dependent effects, which may be important for H_2 in harsh environments.

[6]There are examples of similar associated systems with fine-structure excitation observed in the past (Hamann et al. 2001).

was to derive constraints on the physical conditions in the absorbing medium located near the AGN central engine.

The absorption system consists of three kinematically detached absorption complexes spanning -1700 to -5700 km s^{-1} relative to the QSO redshift. We detected lines profiles of Mg II, Mg I, Ca II, He I*, Mn II, and Fe II. For, the latter species we detected lines from the various fine-structure levels of the ground and second excited electronic states, with energies up to ≈ 8850 cm^{-1}. The lines indicate a partial coverage of the continuum emission source, with a covering factor in the range from 0.98 to 0.2. A relatively simple kinematic structure (in comparison to the majority of known FeLoBALs) and an intermediate saturation allow us to perform joint multicomponent Voigt profile fitting of the aforementioned species (except Mg II) to derive column densities in the simplistic homogeneous partial coverage assumption. Using an additional assumption during the fit, that excitation of Fe II levels dominated by the collisions with electrons, we obtained the constraints on the electron density in the medium to be $\sim 10^4$ cm^{-3} with $\sim$1 dex dispersion. We also detected the lines from the first excited level of Mn II and constrained Mn II*/Mn II column density ratios to be in the range from 0.1 to 0.5 across velocity components. However, the lack of collisional coefficients data for Mn II did not allow us to use Mn II excitation to infer the physical condition in the medium.

Among the other elements detected in this FeLoBAL, He I* is most important since it allows obtaining constraints on the combination of ionization parameter and number density, even without measurement of the hydrogen column density, metallicity, and depletion pattern, which is the case of J 1652+2650. We used CLOUDY code to model the characteristic column densities of He I* and obtained a value of the ionization parameter $\log U \sim -3$ assuming the number density derived from Fe II. Such values are typically measured in FeLoBAL systems, which likely represents the similarity among them, while line profiles in FeLoBALs can be drastically different. With the estimate of the UV flux from J 1652+2650, this translates to a constraint on the distance between the absorbing medium and the continuum source of $\sim$100 pc.

We also discuss the connection of FeLoBAL systems with other types of intrinsic absorbers, including Coronographic and recently identified proximate H$_2$-bearing DLAs. The latter indicates a similar value of the number densities as measured in FeLoBAL, $\gtrsim 10^4$ cm^{-3}. Using CLOUDY modelling we showed that the FeLoBAL and H$_2$-bearing proximate systems located in the adjacent regions in the parameter space, which axes represent the main global characteristics of the medium: thermal pressure and ionization parameter. The same situation is for parameter space representing the number density and the distance to the AGN. This indicates a global natural sequence among associated absorbers, where FeLoBALs represent pre-dominantly gas at the ionization front, Coronographic DLAs are pre-dominantly neutral, and associated H$_2$-bearing absorbers trace the H I-to-H$_2$ transition. This likely will be comprehensively explored with upcoming next-generation wide-field spectroscopic surveys. This shall greatly enhance our understanding of AGN feedback and cool-gas flows from the AGN central engine.

ACKNOWLEDGEMENTS

DATA AVAILABILITY

The data published in this paper are available through Open Access via the ESO scientific archive, and in the SQUAD data base (Murphy et al. 2019). The reduced and co-added spectra can be shared upon request to the corresponding author.

REFERENCES

Aoki K., Oyabu S., Dunn J. P., Arav N., Edmonds D., Korista K. T., Matsuhara H., Toba Y., 2011, PASJ, 63, 457

Arav N., Brotherton M. S., Becker R. H., Gregg M. D., White R. L., Price T., Hack W., 2001, ApJ, 546, 140

Arav N., Moe M., Costantini E., Korista K. T., Benn C., Ellison S., 2008, ApJ, 681, 954

Balashev S. A., Petitjean P., Ivanchik A. V., Ledoux C., Srianand R., Noterdaeme P., Varshalovich D. A., 2011, MNRAS, 418, 357

Balashev S. A. et al., 2017, MNRAS, 470, 2890

Balashev S. A. et al., 2019, MNRAS, 490, 2668

Barlow T. A., Sargent W. L. W., 1997, AJ, 113, 136

Bautista M. A., Dunn J. P., Arav N., Korista K. T., Moe M., Benn C., 2010, ApJ, 713, 25

Becker R. H., Gregg M. D., Hook I. M., McMahon R. G., White R. L., Helfand D. J., 1997, ApJ, 479, L93

Becker R. H., White R. L., Gregg M. D., Brotherton M. S., Laurent-Muehleisen S. A., Arav N., 2000, ApJ, 538, 72

Boroson T. A., Meyers K. A., Morris S. L., Persson S. E., 1991, ApJ, 370, L19

Bowler R. A. A., Hewett P. C., Allen J. T., Ferland G. J., 2014, MNRAS, 445, 359

Brotherton M. S., Arav N., Becker R. H., Tran H. D., Gregg M. D., White R. L., Laurent-Muehleisen S. A., Hack W., 2001, ApJ, 546, 134

Byun D., Arav N., Walker A., 2022a, MNRAS, 516, 100

Byun D., Arav N., Hall P. B., 2022b, MNRAS, 517, 1048

Byun D., Arav N., Hall P. B., 2022c, ApJ, 927, 176

Chaussidon E. et al., 2023, ApJ, 944, 107

Choi H., Leighly K. M., Terndrup D. M., Dabbieri C., Gallagher S. C., Richards G. T., 2022, ApJ, 937, 74

Costa T., Pakmor R., Springel V., 2020, MNRAS, 497, 5229

Crenshaw D. M., Kraemer S. B., Hutchings J. B., Danks A. C., Gull T. R., Kaiser M. E., Nelson C. H., Weistrop D., 2000, ApJ, 545, L27

de Kool M., Arav N., Becker R. H., Gregg M. D., White R. L., Laurent-Muehleisen S. A., Price T., Korista K. T., 2001, ApJ, 548, 609

de Kool M., Becker R. H., Gregg M. D., White R. L., Arav N., 2002a, ApJ, 567, 58

de Kool M., Becker R. H., Arav N., Gregg M. D., White R. L., 2002b, ApJ, 570, 514

Dekker H., D'Odorico S., Kaufer A., Delabre B., Kotzlowski H., 2000, in Iye M., Moorwood A. F., eds, Proc. SPIE Conf. Ser. Vol. 4008, Optical and IR Telescope Instrumentation and Detectors. SPIE, Bellingham, p. 534

Dere K. P., Del Zanna G., Young P. R., Landi E., Sutherland R. S., 2019, ApJS, 241, 22

Drake G. W. F., Morton D. C., 2007, ApJS, 170, 251

Dunn J. P. et al., 2010, ApJ, 709, 611

Elvis M., 2017, ApJ, 847, 56

Everett J., Königl A., Arav N., 2002, ApJ, 569, 671

Farrah D. et al., 2012, ApJ, 745, 178

Fathivavsari H., 2020, ApJ, 888, 85

Fathivavsari H., Petitjean P., Zou S., Noterdaeme P., Ledoux C., Krühler T., Srianand R., 2017, MNRAS, 466, L58

Faucher-Giguère C.-A., Quataert E., 2012, MNRAS, 425, 605

Ferland G. J. et al., 2017, Rev. Mex. Astron. Astrofis., 53, 385

Finley H. et al., 2013, A&A, 558, A111
Fitzpatrick E. L., Massa D., 2007, ApJ, 663, 320
Fynbo J. P. U. et al., 2014, A&A, 572, A12
Gibson R. R. et al., 2009, ApJ, 692, 758
Goodman J., Weare J., 2010, Commun. Appl. Math. Comput. Sci., 5, 65
Hall P. B., Hutsemékers D., Anderson S. F., Brinkmann J., Fan X., Schneider D. P., York D. G., 2003, ApJ, 593, 189
Hamann F. W., Barlow T. A., Chaffee F. C., Foltz C. B., Weymann R. J., 2001, ApJ, 550, 142
Hamann F., Tripp T. M., Rupke D., Veilleux S., 2019, MNRAS, 487, 5041
Hazard C., McMahon R. G., Webb J. K., Morton D. C., 1987, ApJ, 323, 263
Hewett P. C., Foltz C. B., 2003, AJ, 125, 1784
Ishita D., Misawa T., Itoh D., Charlton J. C., Eracleous M., 2021, ApJ, 921, 119
Jin S. et al., 2023, MNRAS, in press
Kling R., Griesmann U., 2000, ApJ, 531, 1173
Knigge C., Scaringi S., Goad M. R., Cottis C. E., 2008, MNRAS, 386, 1426
Korista K. T., Bautista M. A., Arav N., Moe M., Costantini E., Benn C., 2008, ApJ, 688, 108
Kraemer S. B. et al., 2001, ApJ, 551, 671
Krogager J. K. et al., 2023, The Messenger, 190, 38
Leighly K. M., Dietrich M., Barber S., 2011, ApJ, 728, 94
Liu W.-J. et al., 2015, ApJS, 217, 11
Lucy A. B., Leighly K. M., Terndrup D. M., Dietrich M., Gallagher S. C., 2014, ApJ, 783, 58
Morton D. C., 2003, ApJS, 149, 205
Murphy M. T., Bernet M. L., 2016, MNRAS, 455, 1043
Murphy M. T., Kacprzak G. G., Savorgnan G. A. D., Carswell R. F., 2019, MNRAS, 482, 3458
Nave G., Johansson S., 2013, ApJS, 204, 1
Negrete C. A. et al., 2018, A&A, 620, A118

Noterdaeme P., Balashev S., Krogager J. K., Srianand R., Fathivavsari H., Petitjean P., Ledoux C., 2019, A&A, 627, A32
Noterdaeme P., Balashev S., Krogager J. K., Laursen P., Srianand R., Gupta N., Petitjean P., Fynbo J. P. U., 2021, A&A, 646, A108
Noterdaeme P. et al., 2023, A&A, 673, A89
Pâris I. et al., 2018, A&A, 613, A51
Proga D., Stone J. M., Kallman T. R., 2000, ApJ, 543, 686
Reichard T. A. et al., 2003, AJ, 125, 1711
Safronova M. S., Safronova U. I., 2011, Phys. Rev. A, 83, 012503
Sarazin M., Roddier F., 1990, A&A, 227, 294
Schnabel R., Schultz-Johanning M., Kock M., 2004, A&A, 414, 1169
Selsing J., Fynbo J. P. U., Christensen L., Krogager J. K., 2016, A&A, 585, A87
Shen Y. et al., 2016, ApJ, 831, 7
Smith P. S., Schmidt G. D., Allen R. G., Angel J. R. P., 1995, ApJ, 444, 146
Tolea A., Krolik J. H., Tsvetanov Z., 2002, ApJ, 578, L31
Trump J. R. et al., 2006, ApJS, 165, 1
Veilleux S., Meléndez M., Tripp T. M., Hamann F., Rupke D. S. N., 2016, ApJ, 825, 42
Véron-Cetty M. P., Véron P., 2010, A&A, 518, A10
Walker A., Arav N., Byun D., 2022, MNRAS, 516, 3778
Wampler E. J., Chugai N. N., Petitjean P., 1995, ApJ, 443, 586
Weselak T., Galazutdinov G. A., Musaev F. A., Beletsky Y., Krełowski J., 2009, A&A, 495, 189
Weymann R. J., Carswell R. F., Smith M. G., 1981, ARA&A, 19, 41
Xu X., Arav N., Miller T., Korista K. T., Benn C., 2021, MNRAS, 506, 2725

APPENDIX A: CA II, MG I, AND HE I⋆ FITS

Here, we present the figures of all the fitted Ca II, Mg I, He I⋆, Fe II, and Mn II lines.
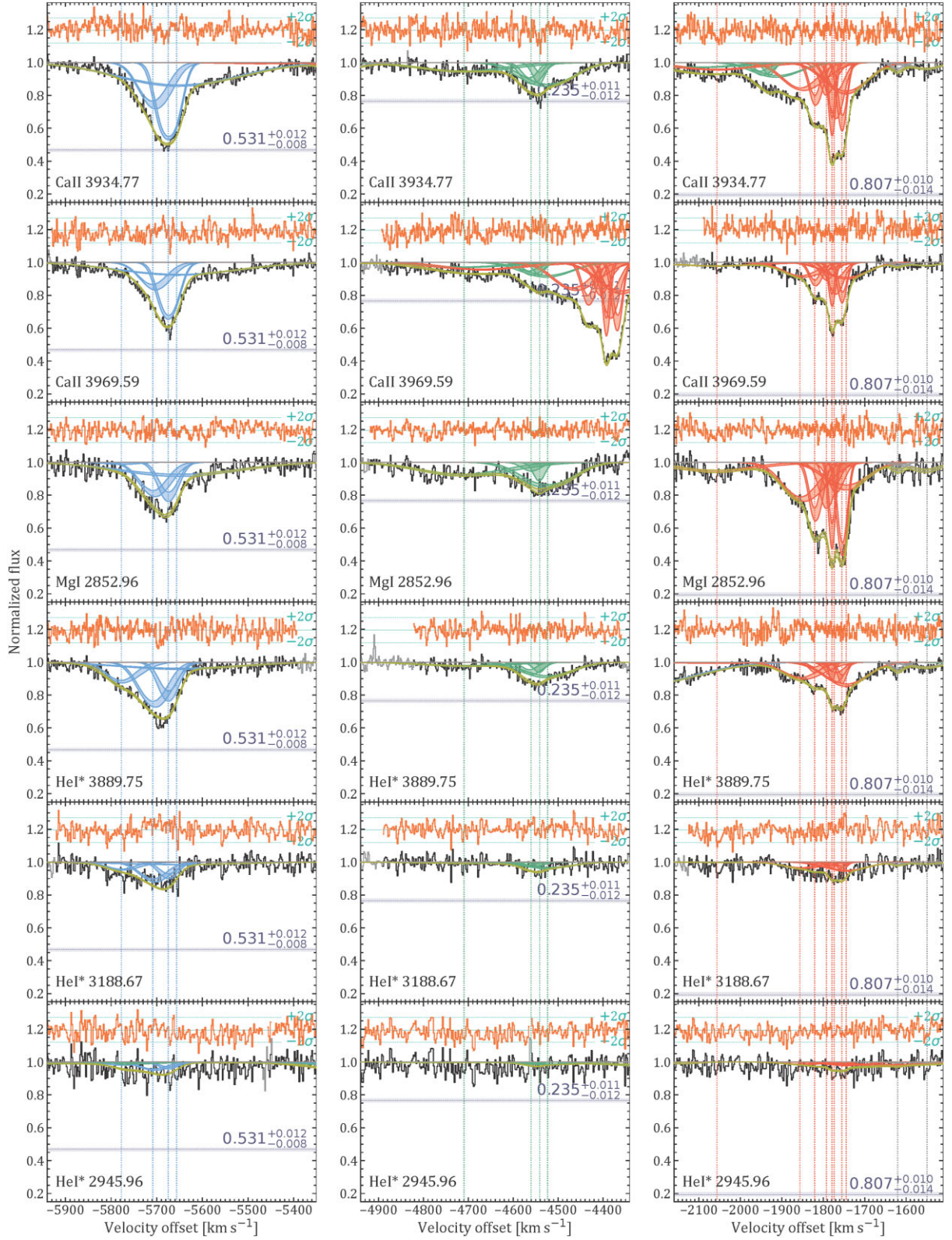
Figure A1. *Left to right*: Voigt-profile fits to Ca II, Mg I, and He I⋆ absorption lines in complexes *A* (left), *B* (middle), and *C* (right), at $z_{abs} = 0.3253$, 0.3304, and 0.3429, respectively, towards J 1652+2650. The graphical information is the same as in Fig. 4. The red lines at the top of each panel show the residuals between the spectrum and fit, with the green dashed horizontal lines corresponding to 2σ deviation.
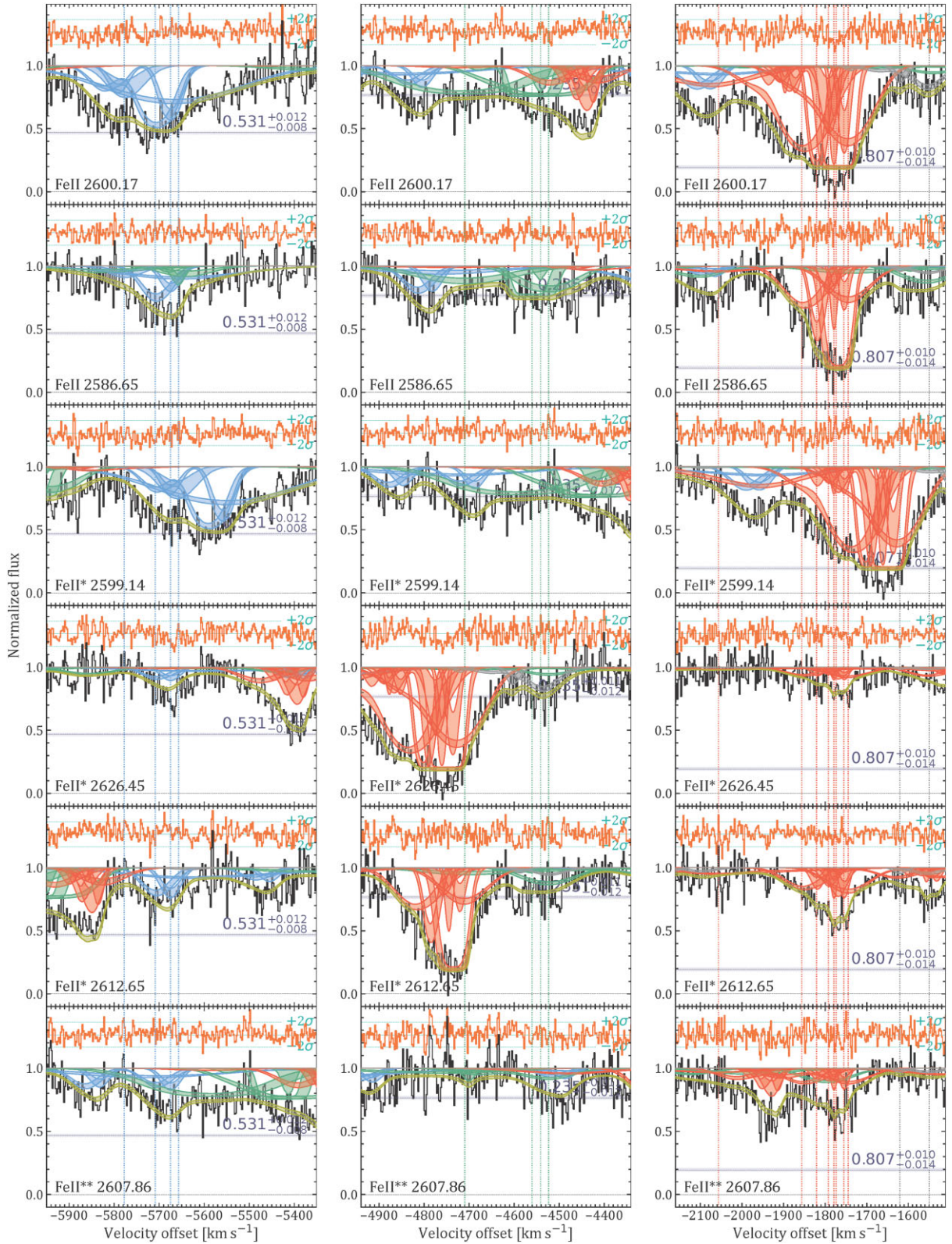
Figure A2. *Left to right*: Voigt-profile fits to Fe II absorption lines in complexes *A* (left), *B* (middle), and *C* (right), at $z_{abs} = 0.3253$, 0.3304, and 0.3429, respectively, towards J 1652+2650. The horizontal dashed lines and surrounding grey areas indicate the extent of partial covering determined by fitting each clump independently with its own covering factor.
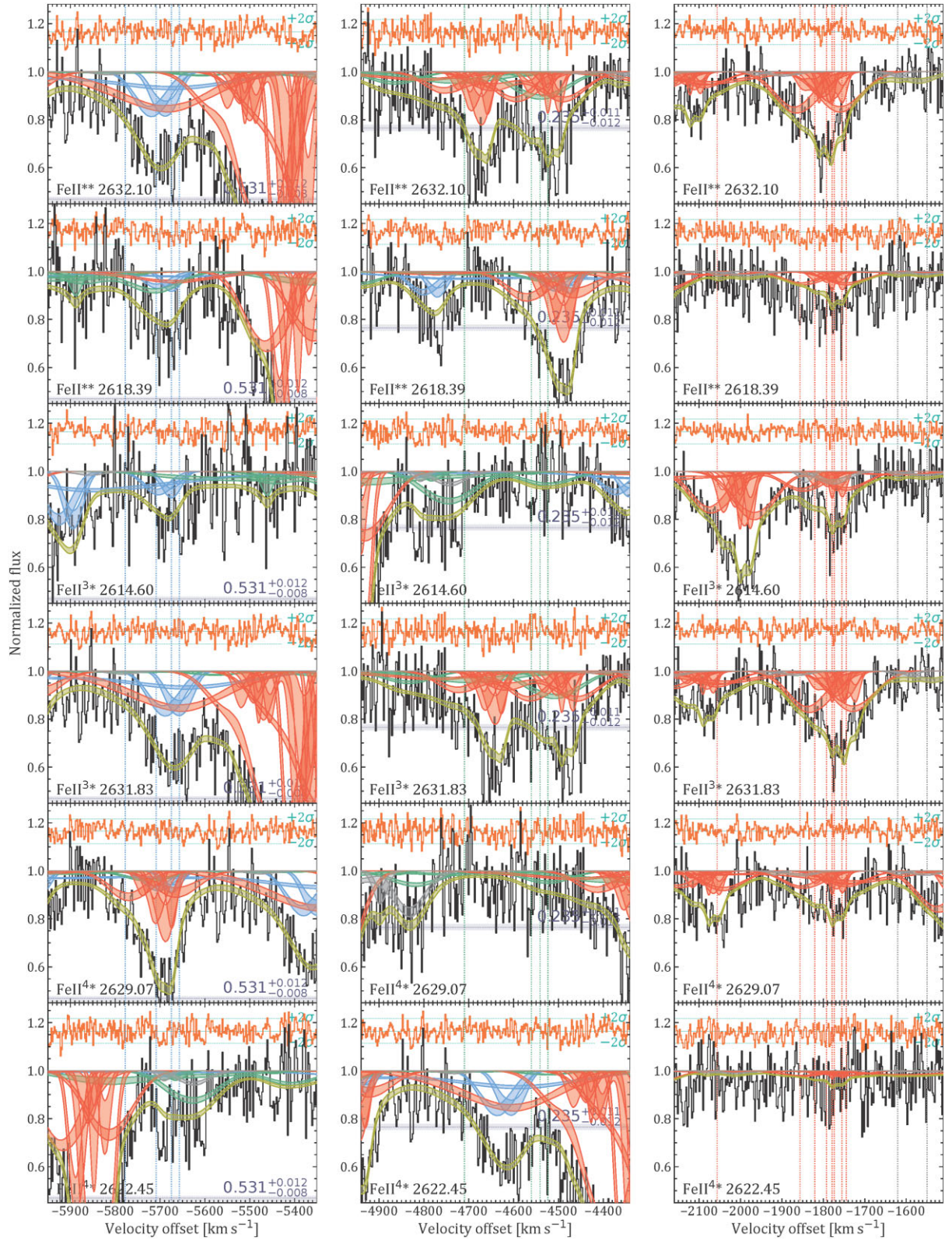
Figure A3. Same as Fig. A2 for higher excitation Fe II lines.
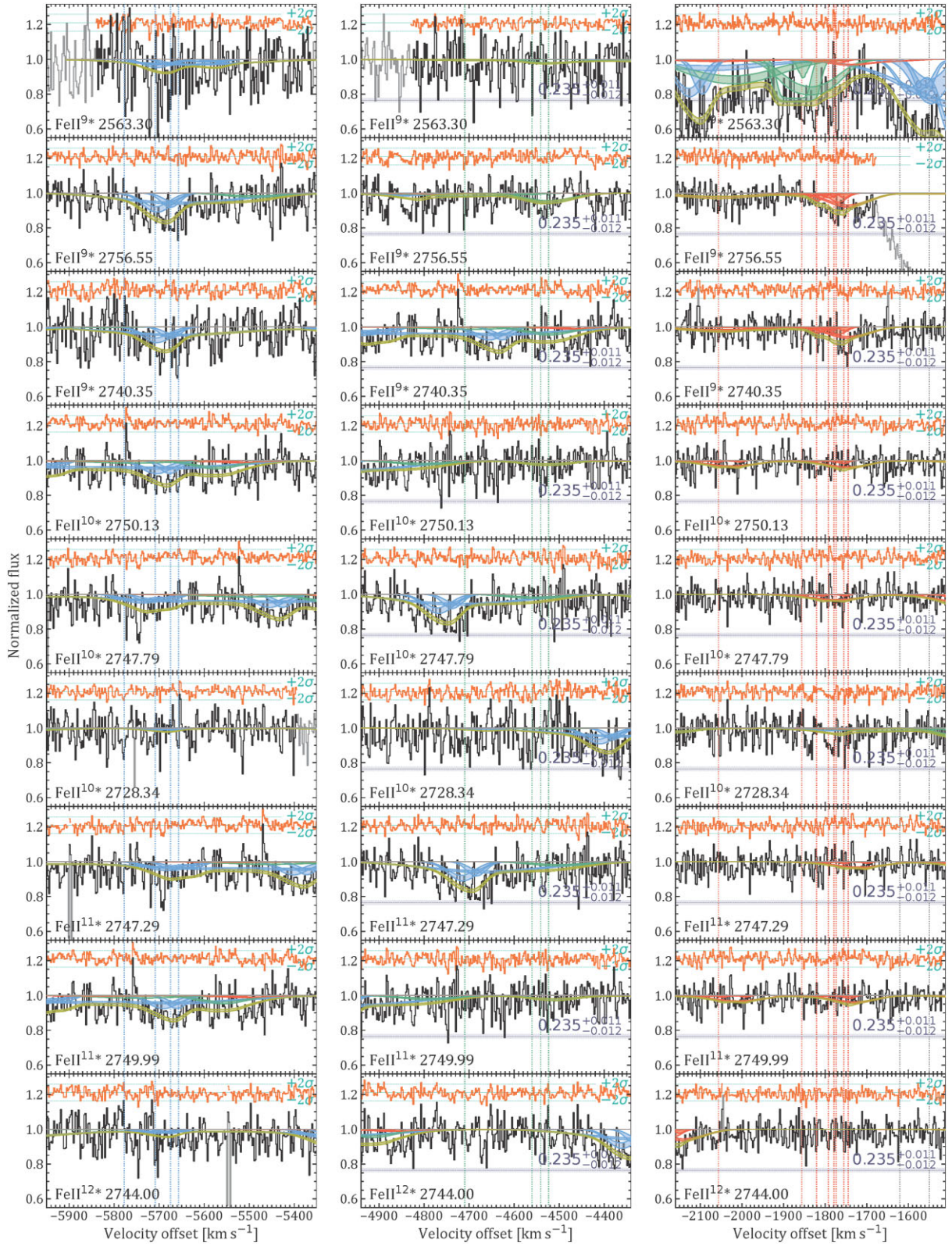
Figure A4. Same as Fig. A2 for higher excitation Fe II lines (continued).
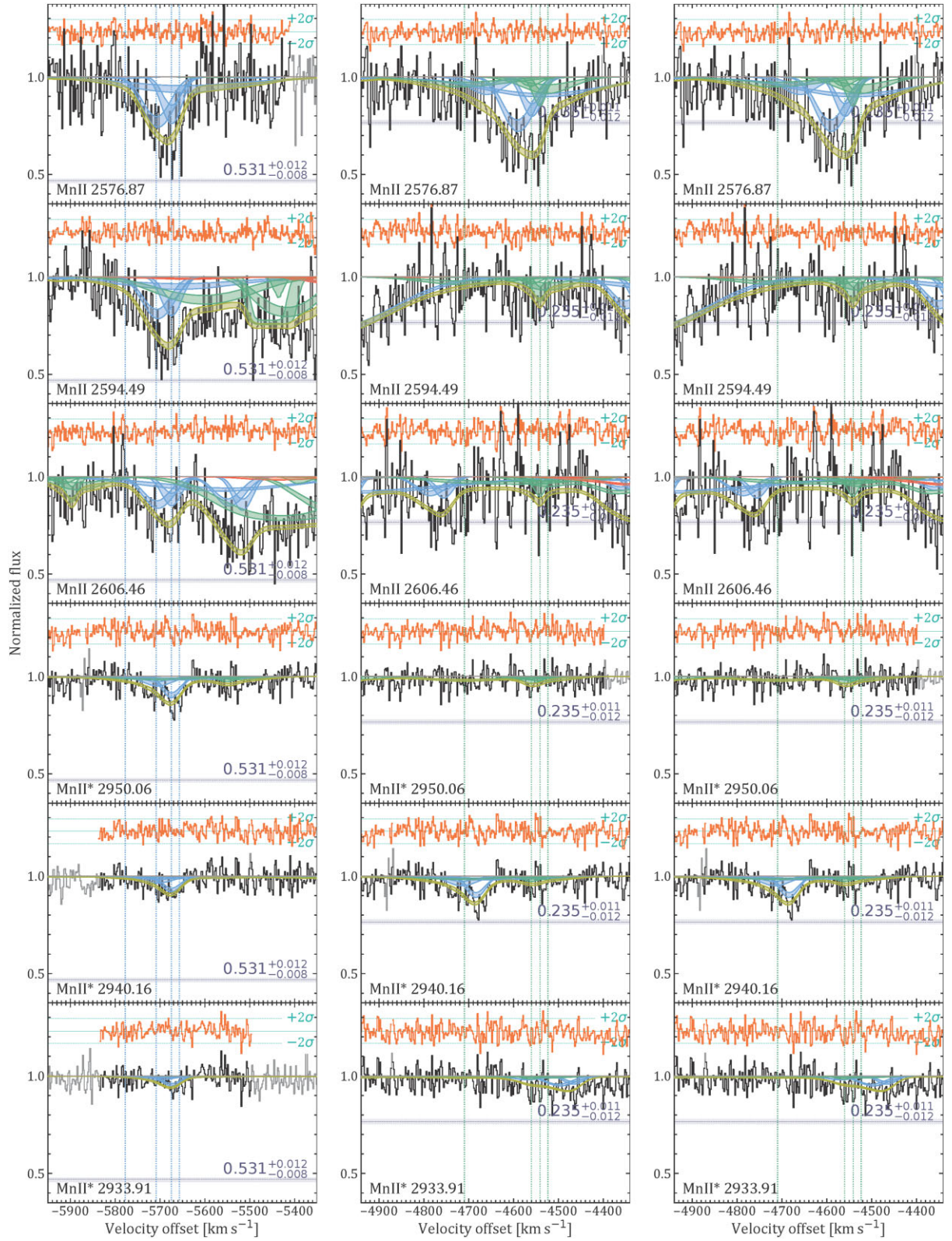
Figure A5. Same as Fig. A2 for Mn II lines.
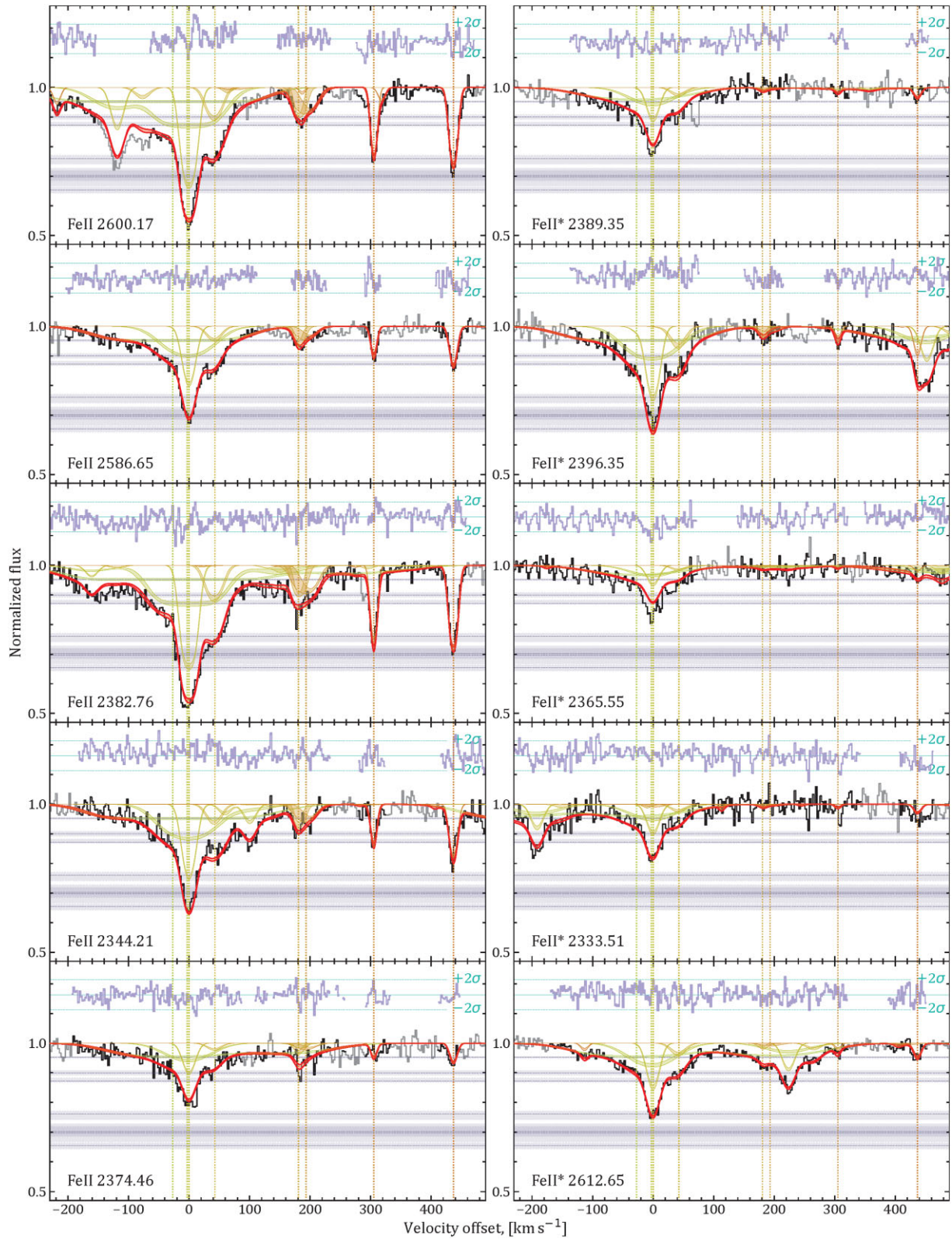
Figure A6. Voigt-profile fits to Fe II absorption lines at $z_{abs} = 0.85993$ towards Q 2359−1241. The graphical information is similar to that in Fig. A1.
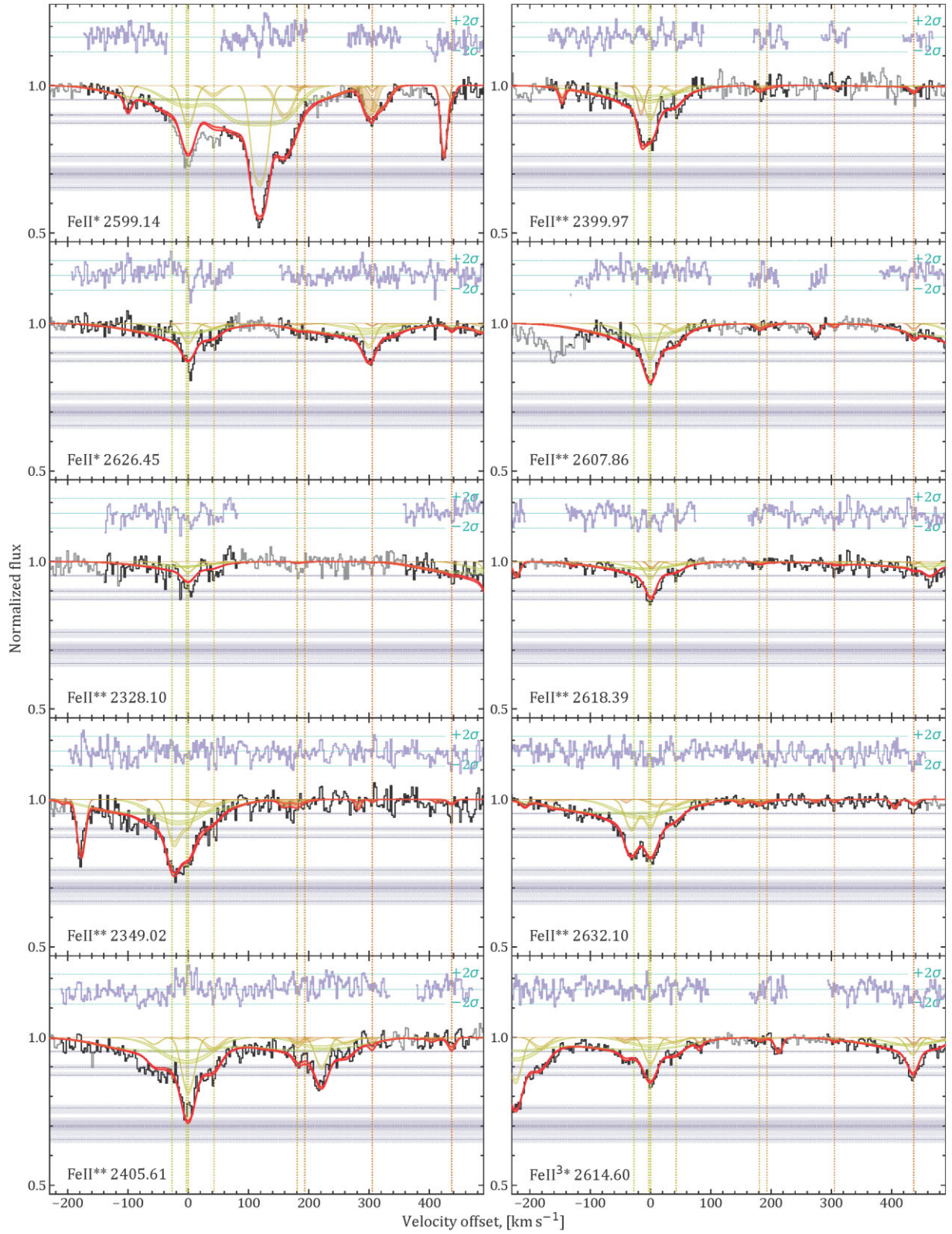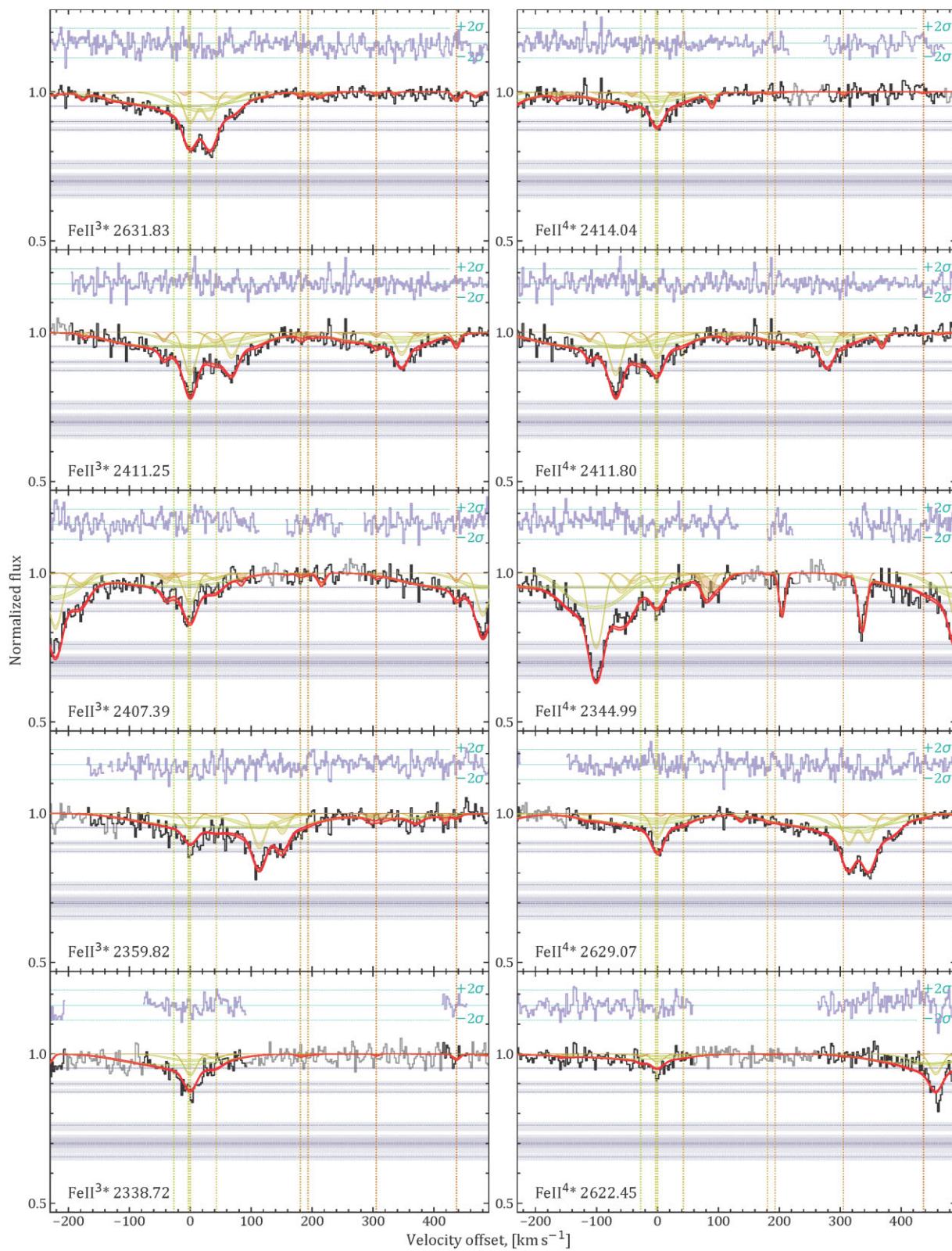
Figure A7. Same as Fig. A6 for higher excitation Fe II lines.

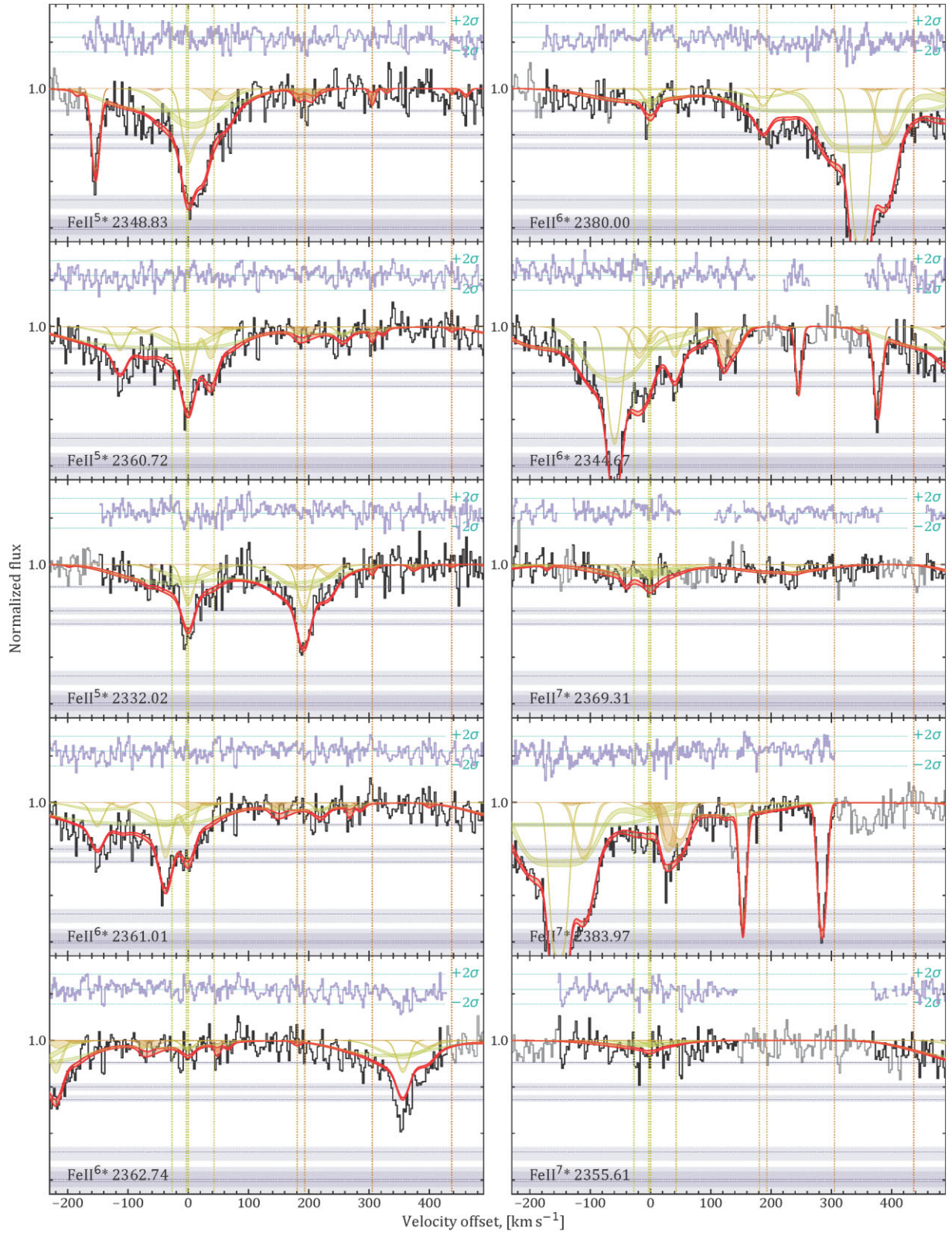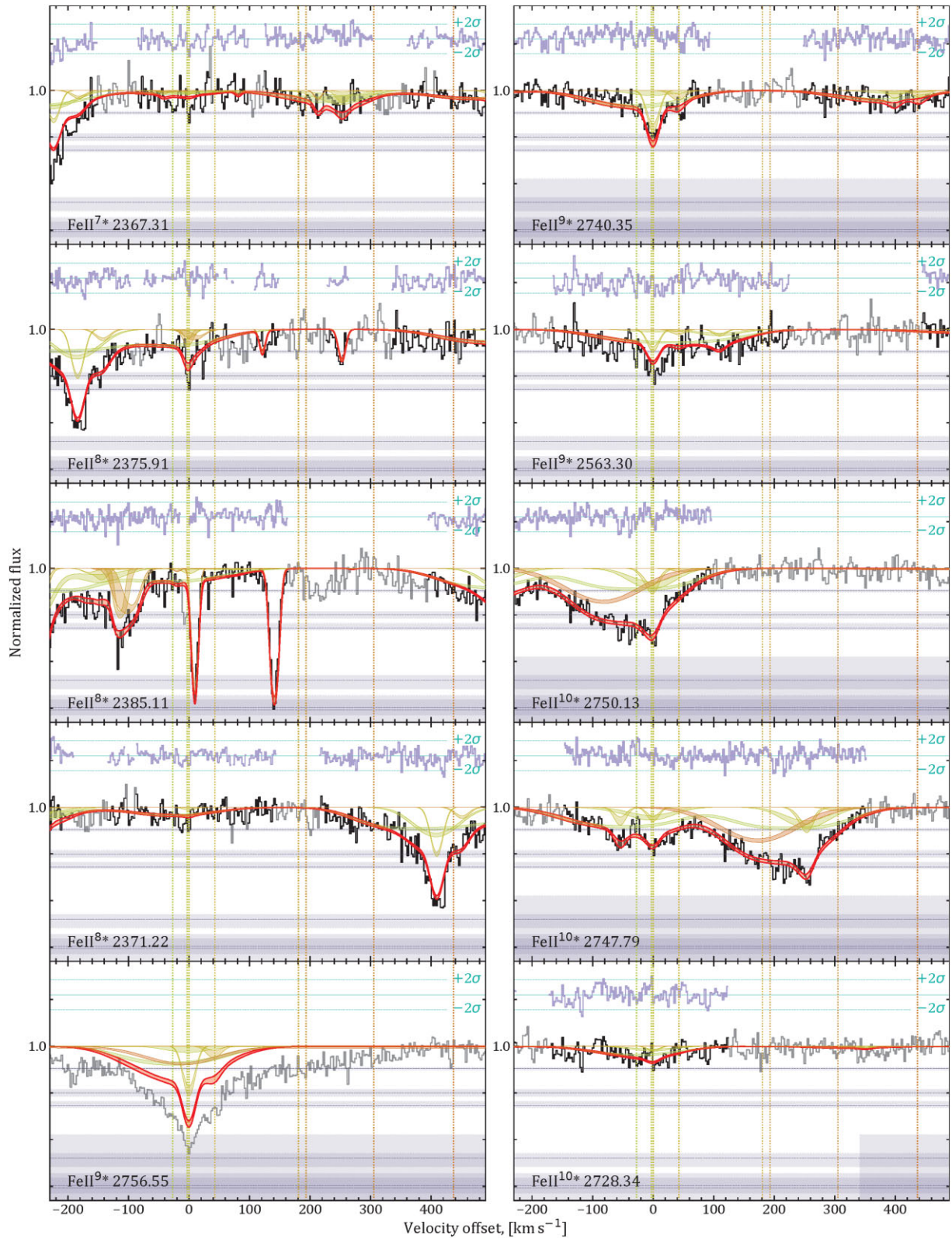**Figure A8.** Same as Fig. A6 for higher excitation Fe II lines (continued).

Figure A9. Same as Fig. A6 for higher excitation Fe II lines (continued).

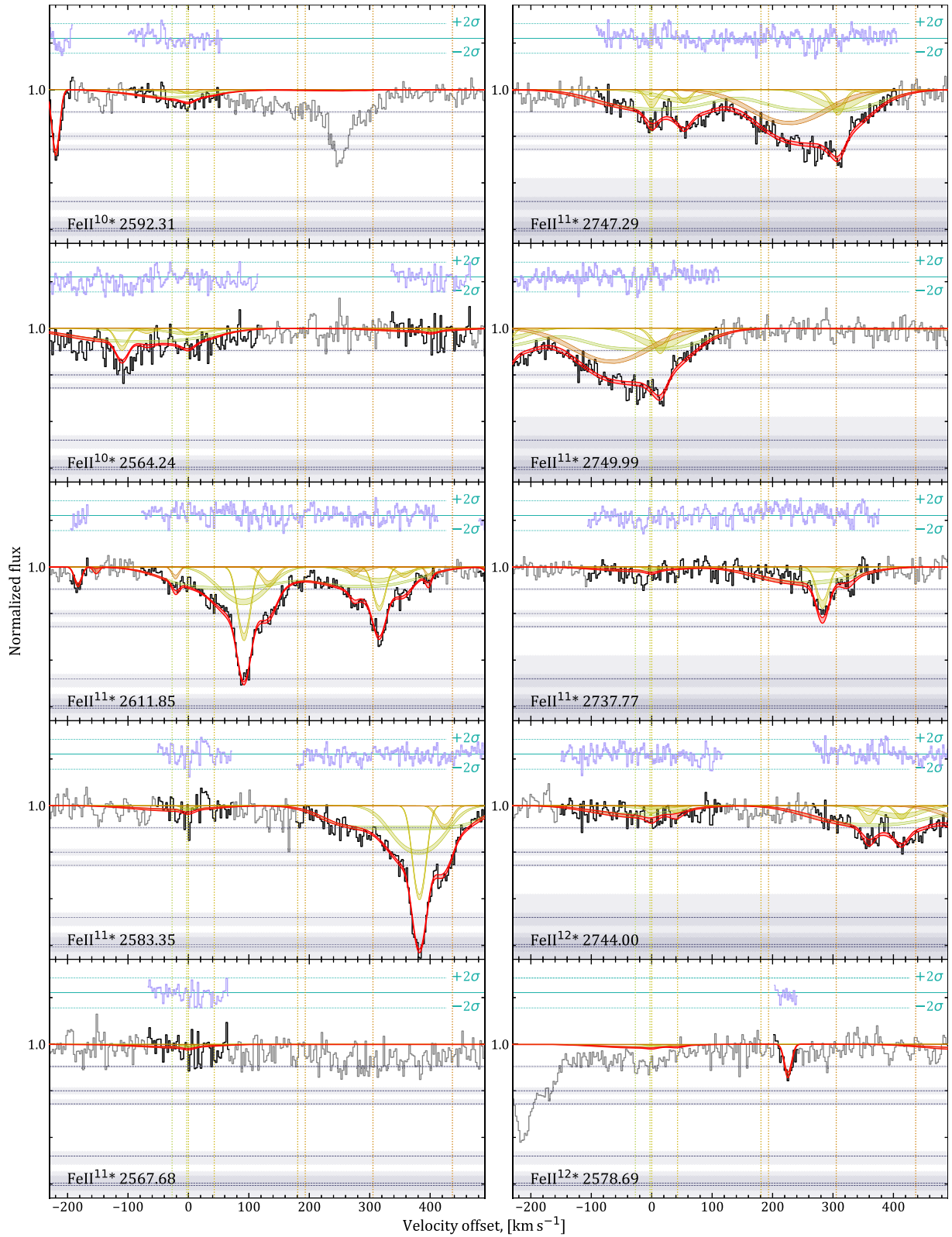**Figure A10.** Same as Fig. A6 for higher excitation Fe II lines (continued).

Figure A11. Same as Fig. A6 for higher excitation Fe II lines (continued).

This paper has been typeset from a TEX/LATEX file prepared by the author.